Seasonal Cycle of Mesoscale Instability of the West Spitsbergen Current

Wilken-Jon von Appen and Ursula Schauer

Alfred Wegener Institute, Helmholtz Centre for Polar and Marine Research, Bremerhaven, Germany

Tore Hattermann

Alfred Wegener Institute, Helmholtz Centre for Polar and Marine Research, Bremerhaven, Germany, and Akvaplan-niva AS, Tromsø, Norway

Agnieszka Beszczynska-Möller

Institute of Oceanology, Polish Academy of Sciences, Sopot, Poland

ABSTRACT

The West Spitsbergen Current (WSC) is a topographically steered boundary current that transports warm Atlantic Water northward in Fram Strait. The 16 yr (1997–2012) current and temperature–salinity measurements from moorings in the WSC at 78°50′N reveal the dynamics of mesoscale variability in the WSC and the central Fram Strait. A strong seasonality of the fluctuations and the proposed driving mechanisms is described. In winter, water is advected in the WSC that has been subjected to strong atmospheric cooling in the Nordic Seas, and as a result the stratification in the top 250 m is weak. The current is also stronger than in summer and has a greater vertical shear. This results in an *e*-folding growth period for baroclinic instabilities of about half a day in winter, indicating that the current has the ability to rapidly grow unstable and form eddies. In summer, the WSC is significantly less unstable with an *e*-folding growth period of 2 days. Observations of the eddy kinetic energy (EKE) show a peak in the boundary current in January–February when it is most unstable. Eddies are then likely advected westward, and the EKE peak is observed 1–2 months later in the central Fram Strait. Conversely, the EKE in the WSC as well as in the central Fram Strait is reduced by a factor of more than 3 in late summer. Parameterizations for the expected EKE resulting from baroclinic instability can account for the observed EKE values. Hence, mesoscale instability can generate the observed variability, and high-frequency wind forcing is not required to explain the observed EKE.

1. Introduction

The Arctic Ocean's volume, heat, and freshwater budget depend upon the oceanic exchanges with the lower-latitude ocean. Fram Strait between Greenland and Svalbard is the widest and deepest strait of the Arctic Ocean. On its western side is the 250-km-wide east Greenland shelf (depth 50–200 m), in the center is the 270-km-wide deep part of the strait (depth ≈ 2500 m),

and in the east is the 40-km, narrow West Spitsbergen shelf. The continental margins connecting these regions support boundary currents. The East Greenland Current (EGC) is the boundary current along the east Greenland continental margin that advects polar outflow water as well as sea ice southward. The West Spitsbergen Current (WSC) is the boundary current along the West Spitsbergen continental margin (Aagaard et al. 1987). It transports warm (2°–6°C in summer, 2°–4°C in winter; Beszczynska-Möller et al. 2012) Atlantic Water (AW) northward that entered the Nordic Seas from the North Atlantic and traveled northward in the Norwegian Atlantic Current. On this pathway, the AW is subject to intense atmospheric cooling (latent and sensible heat fluxes), especially in winter (Boyd and D'Asaro 1994). Furthermore, horizontal eddy fluxes between the warm AW boundary current in the eastern Nordic Seas and the

interior basins have been identified as crucial for the cooling of the boundary current along its cyclonic pathway around the Nordic Seas (Spall 2011). By shedding eddies, warm water is moved from the swift boundary current to the interior basins and thereby the surface area and thus the time for cooling of AW at this latitude is enlarged significantly. It is therefore important to understand the mechanisms of these eddy fluxes that depend on the stability of the boundary currents.

To learn more about the meridional water exchange and oceanic heat transport into the Arctic Ocean, the Alfred Wegener Institute (AWI) and the Norwegian Polar Institute (NPI) have been maintaining a mooring array across the deep Fram Strait at 78°50′N since 1997. The mean northward volume transport in the WSC at this latitude was determined to be 6.6 ± 0.4 Sverdrups (Sv; $1 \, \text{Sv} \equiv 10^6 \, \text{m}^3 \, \text{s}^{-1}$; Beszczynska-Möller et al. 2012). The variability of the transport is largest in the offshore side of the WSC (termed offshore branch) where the transport can differ by up to 3–4 Sv between months. The temperature of the Atlantic Water increased over the observation period up until 2007 (Beszczynska-Möller et al. 2012) and has since stayed at that elevated level.

The warm water supply to the Arctic Ocean is responsible for the local ice melt north of Svalbard and the halocline formation there (Rudels et al. 2005). Once the halocline has been formed, the AW underneath is mostly isolated from the atmosphere. The AW then circulates around the Arctic Ocean as a cyclonic boundary current (Rudels et al. 1994, 1999; Woodgate et al. 2001; Aksenov et al. 2011) before finally exiting the Arctic Ocean through the western Fram Strait.

In Fram Strait, some of the AW flows northward into the Arctic Ocean and another part flows westward in the so-called Atlantic Water recirculation toward the southward-flowing EGC (Bourke et al. 1988). Using pairs of shore to shore conductivity–temperature–depth (CTD) sections at different latitudes throughout 4 yr, the strength of the recirculation was inferred as the amount of flow that did not make it to the northern section of the pairs (Marnela et al. 2013). This assumes fully geostrophic flows and finds a recirculation transport of 2 Sv in summer. The relocation of the western (NPI) part of the Fram Strait mooring array from 79° to 78°50′N showed that the southward transport of the EGC increases by 3 Sv in this 10′ latitudinal band (18 km; de Steur et al. 2014). Unlike in the halocline formation region north of Svalbard (Rudels et al. 2005), the AW flowing westward in the recirculation actually has to subduct under the polar outflow. Since potential vorticity dynamics inhibit vertical motion in steady flows, a mechanism is required for those vertical motions to occur and eddies have been suggested to be able to

achieve this (Hattermann et al. 2016, manuscript submitted to *Geophys. Res. Lett.*).

The mesoscale eddy field in Fram Strait has been studied in the 1980s as part of the Marginal Ice Zone Experiment (Johannessen et al. 1983, 1987). Long-lived eddies were observed then as well as large features (compared to the Rossby radius of deformation) such as a cyclonic circulation seemingly associated with the f/H (where f is the Coriolis parameter and H is the depth) contours of the Molloy Hole (Manley et al. 1987; Quadfasel et al. 1987). However, the eddy field has, to date, not been sampled at resolutions comparable to the Rossby radius. Mooring observations in the WSC in the late 1970s suggested that the WSC is baroclinically unstable and barotropically stable (Hanzlick 1984). However, the variability could not be sufficiently quantified to assess the instabilities' importance compared to other forcing mechanisms. An idealized model of the WSC was fitted to 1 and 2 yr of observations from the same moored array as in this study. It was shown that the WSC is baroclinically and barotropically unstable during some of the studied times (Teigen et al. 2010, 2011) and that the baroclinically unstable conditions appeared to occur more often in winter. Eddy variability in Fram Strait was also linked to the propagation of linear small-amplitude shelf waves along the West Spitsbergen margin (Nilsen et al. 2006) and to the generation through strong local wind forcing (Jónsson et al. 1992).

The northward transport, that is, toward the Arctic Ocean, of heat in the Atlantic layer depends on heat loss to the atmosphere and on eddy fluxes. Eddies may exchange water with different properties between a boundary current and the interior ocean without changing the volume transport in the boundary current. However, eddies can also contribute to the weakening of the boundary current resulting in a decrease of the volume transport in the boundary current. The latter mechanism seems to be one of the drivers of the westward recirculation of Atlantic Water in Fram Strait (Gascard et al. 1995; Hattermann et al. 2016, manuscript submitted to *Geophys. Res. Lett.*). Furthermore, the meridional exchange flow at depth (≈2000–2500 m) in the Fram Strait appears to be eddy driven (von Appen et al. 2015b).

In the Labrador Sea, the observed level and seasonal cycle of eddy kinetic energy (EKE) in the West Greenland Current, another high-latitude boundary current, has been explained entirely by mesoscale instability of the boundary current, and high-frequency winds were not required (Eden and Böning 2002). Here, we ask if the situation in Fram Strait is similar to the Labrador Sea and is the EKE observed in Fram Strait mainly due to boundary current instability processes without depending on high-frequency wind

TABLE 1. Deployment details of the 19 moorings considered in this study. Over the years, the mooring and instrument locations slightly varied as indicated by the ranges. The ranges of the instrument depths for the upper level and the middepth level are given in the table and in the text these levels are called 75-m level and 250-m level for ease of notation. The duration of the temperature and velocity measurements is given as is the duration of the salinity measurements at the two levels (longer records at the upper level).

Name	Longitude	Latitude	Water depth (m)	Upper level (m)	Middepth level (m)	Temperature/velocity duration	Salinity duration (upper level) (yr)	Salinity duration (middepth level) (yr)
F1	8°38′–8°40′E	78°50′–78°50′N	204–308	44–95	204–283	1997–2009	7	4
F2	8°18′–8°21′E	78°50′–78°52′N	746–801	52–102	234–296	1997–2012	12	4
F3	7°57′–8°00′E	78°50′–78°51′N	1000–1043	61–118	250–314	1997–2012	8	4
F4	6°55′–7°01′E	78°50′–78°50′N	1354–1527	51–115	215–297	1997–2012	11	1
F5	5°51′–6°28′E	78°49′–78°50′N	1993–2500	53–116	231–316	1997–2012	10	2
F6	5°00′–5°03′E	78°50′–78°50′N	2667–2698	48–101	206–305	1997–2012	13	3
F7	4°00′–4°05′E	78°49′–78°51′N	2302–2346	53–99	252–298	1997–2010	13	—
F8	2°34′–2°48′E	78°50′–78°50′N	2463–2505	56–101	241–303	1997–2012	13	—
F15	1°36′–1°37′E	78°50′–78°50′N	2504–2529	49–134	233–294	2002–12	9	—
F16	0°23′–0°32′E	78°50′–78°50′N	2550–2567	50–132	238–312	2002–12	9	—
F9	0°49′W–0°16′E	78°50′–79°00′N	2489–2656	54–118	237–337	1997–2012	12	—
F10	2°07′–2°00′W	78°49′–79°01′N	2589–2702	64–101	256–280	1997–2012	13	—
F11	3°38′–3°01′W	78°48′–79°01′N	2126–2503	45–114	180–307	1998–2012	12	4
F12	4°15′–3°52′W	78°48′–79°00′N	1807–2017	27–79	279–359	1997–2012	10	2
F13	5°21′–4°59′W	78°50′–78°58′N	970–1039	47–75	224–272	1997–2012	10	2
F14	6°51′–6°27′W	78°49′–79°02′N	263–284	50–95	264–284	1997–2012	12	1
HS	5°02′–5°05′E	78°35′–78°35′N	2225–2334	—	219–288	2006–08	—	—
HC	4°20′–4°21′E	79°00′–79°01′N	2521–2584	—	135–277	2006–14	—	3
HN	4°04′–4°30′E	79°44′–79°44′N	2537–2774	—	214–381	2007–14	—	3

forcing? This paper provides an improved understanding of the mesoscale dynamics in Fram Strait by analyzing a wealth of observations in Fram Strait: 16 yr of mooring data, annual hydrographic sections, Argo floats, and satellite altimetry. This allows us to describe the seasonal variation of the EKE generated by the WSC and thus to understand the reasons for that progression, specifically whether it can be explained by oceanic processes. Section 2 introduces the different datasets used in this study. The seasonality of hydrography and velocity in the WSC from observations is presented in section 3. Observational diagnostics of mesoscale instabilities in the WSC are shown in section 4. The observed quantities are used in section 5 to assess the level of EKE expected solely from oceanic processes. A discussion in section 6 concludes this study.

2. Data and methods

a. Temperature, salinity, and velocity time series from moorings

From 1997 onward, a mooring array as well as three individual moorings have been maintained in Fram Strait (Table 1) by the physical oceanography group of the Alfred Wegener Institute (F1–F10 and F15/F16; Beszczynska-Möller et al. 2012), the Norwegian Polar Institute (F11–F14; de Steur et al. 2009), and the Hausgarten Deep Sea Observatory group of the Alfred Wegener Institute [Hausgarten South (HS), Hausgarten Central (HC), Hausgarten North (HN); Bauerfeind et al. 2009]. Except for the Hausgarten moorings, the moorings are deployed along a zonal section along 78°50′N (Fig. 1). However, up until 2002, the westernmost part of the array (F9–F14) was located at 79°N and at 78°50′N thereafter. For the analysis of Fig. 2 (below), the moorings at different latitudes are considered as individual time series, while the analyses of Figs. 8 and 9 (below) only use the data at 78°50′N. Here, we use the data until 2012 from the zonal array and until 2014 from the Hausgarten moorings. The mooring data are available through the data publisher PANGAEA (Beszczynska-Möller et al. 2015; Bauerfeind et al. 2015).

The moorings along 78°50′N measured temperature and velocity at five standard depths: ≈75 m, ≈250 m, ≈750 m, and ≈1500 m below the surface and ≈10 m above the bottom. The Hausgarten moorings only contained instruments ≈250 m below the surface and ≈10 m above the bottom. The temporal resolution ranged from 20 min to 2 h. Salinity was measured in 75-m depth along 78°50′N. Additionally, salinity has been measured in 250-m depth on the eastern six moorings (F1–F6) since 2008. Because of various instrument and mooring failures, the records are not complete in all years. The salinity records in ≈250 m in the WSC are at least 1 yr long (Table 1) and at least 7 yr in ≈75 m. The temperature
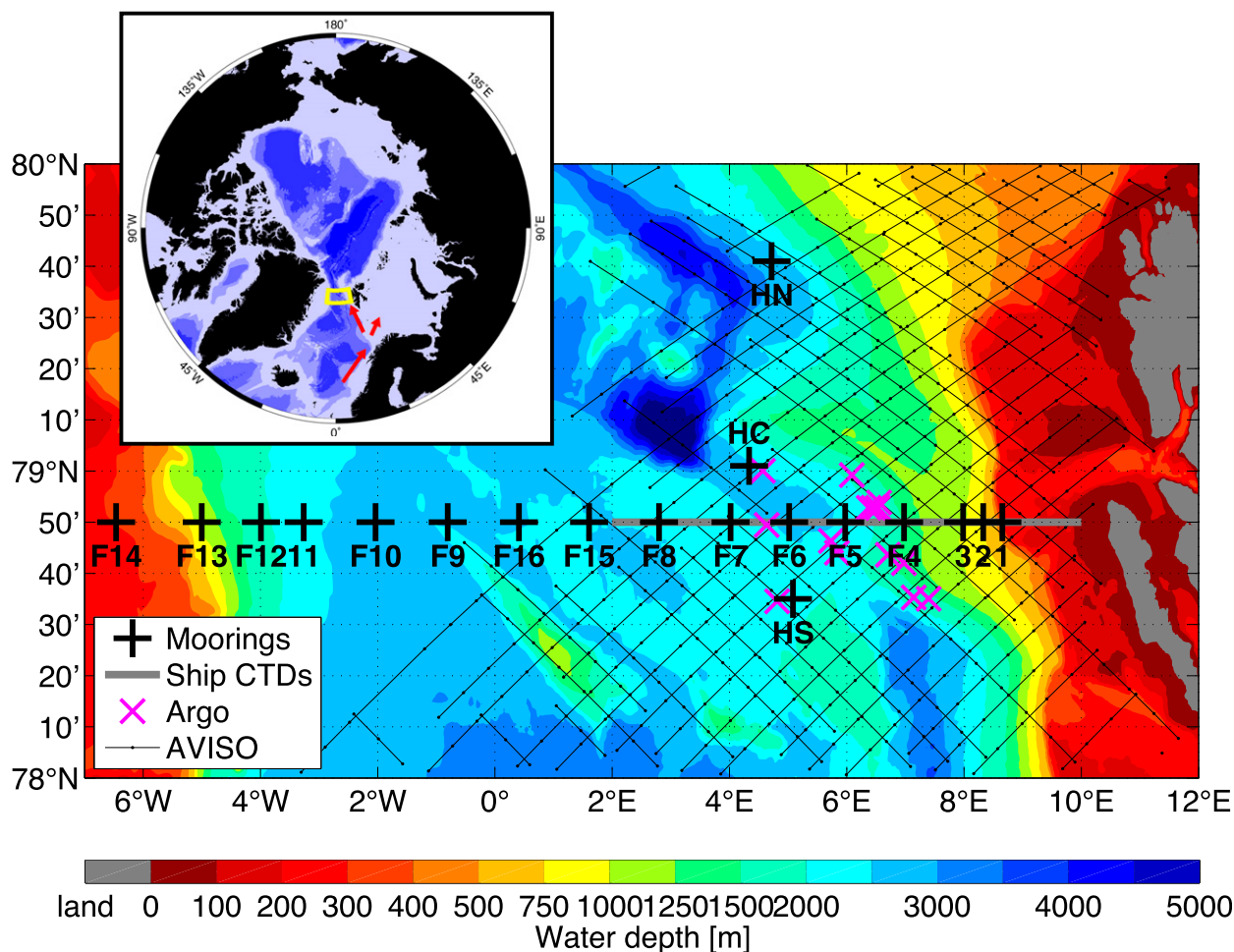
FIG. 1. Map of data distribution in Fram Strait. Water depths (color) are from IBCAO, version 3.0 (Jakobsson et al. 2012). The locations of the moorings are shown as black +. The repeat CTD section used in this study along 78°50′N is indicated by the gray line. The locations of the 14 Argo profiles used in this study are shown as magenta X. The thin black lines are repeat cycle 90 of the *Envisat* altimeter that shows a typical coverage of the repeat cycles in the Fram Strait region. The inset in the top-left corner shows the whole Arctic. The extent of the main map is shown as a yellow polygon. The pathways of Atlantic Water along the Norwegian continental margin, into the Barents Sea, and along the West Spitsbergen continental margin are shown schematically.

and velocity record lengths all exceed 12 yr. Vertical mooring motion (blowdown) due to strong horizontal currents occurred occasionally at individual moorings. To avoid biasing long-term temperature or salinity means, we excluded temperature and salinity data measured more than 30 m below the planned deployment depth when calculating temperature and salinity statistics. The moored temperature and salinity time series were checked for offsets and drifts by comparison to shipboard CTD data (section 2b). If a time series exhibited an offset or drift, it was removed. No further filtering was applied, but, as stated below, most of the analyses are based on 2-day low-pass filtered data. The majority of the array has consisted of Aanderaa current meters (rotor current meters: RCM7 and RCM8; Doppler current meter: RCM11) often measuring pressure

and always measuring speed, direction, and temperature. Salinity has been measured by Seabird SBE16 Seacats and SBE37 Microcats, and these instruments also measured temperature and pressure. Starting in 2011, some of the moorings have also been equipped with a RDI 150 kHz QuarterMaster Workhorse ADCP looking upward from 250-m depth. Here, we only use a 1 yr ADCP record from mooring F6 (Fig. 7 below).

b. Shipboard CTD profiles

A section of CTD profiles in Fram Strait along 78°50′N (Fig. 1) has been occupied every summer since 1997 as part of the mooring service cruises by the research vessels *Polarstern*, *Merian*, and *Lance*. Seabird 911+ systems were used, and standard precruise plus bottle salinity calibration was applied to all of the

profiles. The data from all of these CTD sections are available in PANGAEA (von Appen et al. 2015a).

c. CTD profiles from Argo floats

Six Argo[1] floats (WMO numbers 6900218, 6900303, 6900328, 6900331, 6900335, and 6900345) made it into the eastern Fram Strait in the years 2006, 2007, 2008, and 2011. They measured 14 hydrographic profiles between the surface and 2000-m depth within 0.25° latitudinally of the mooring array (Fig. 1). The delayed-mode, quality-controlled data (processed as described in Latarius and Quadfasel 2010) are used (NODC 2015).

d. Sea surface height from satellite along-track altimetry

The *Environmental Satellite* (*Envisat*) of the European Space Agency is the only satellite[2] whose orbit reaches far enough north to cover the Fram Strait region. The delayed-time along-track (level 2) data of sea surface height (SSH) were downloaded from AVISO for the years 2002–12. The altimeter products were produced by Ssalto/Duacs and distributed by AVISO, with support from CNES (AVISO 2015). The analysis was carried out in 21-km zonal width by 18-km meridional width bins. Bins that were in the ice or less than 20 km from the ice edge in Fram Strait, as determined from the satellite microwave ice concentration (section 2e), were excluded from the analysis as the sea ice freeboard contaminates the signal of the water surface. The typical along-track coverage of the *Envisat* satellite is illustrated by one repeat cycle (Fig. 1). The coverage varies a bit between repeat cycles, but over the WSC the coverage is very good because the ice edge is located in the center of Fram Strait most of the time (Fig. 9).

e. Sea ice concentration from satellite microwave sensors

For information on sea ice concentration, we use the data, when available, from the Advanced Microwave Scanning Radiometer sensors AMSR-E and AMSR-2 (University of Bremen 2015a,b) for the years 2004–13 (Spreen et al. 2008). We identified the position of the

sea ice edge as the line with a concentration exceeding 50%. We note that due to the sharpness of the sea ice edge in Fram Strait, the ice edge determination is not very sensitive to the choice of the cutoff sea ice concentration.

f. Sea surface temperature from satellite infrared and microwave sensors

Sea surface temperature was taken from the blended product of satellite infrared observations (AVHRR) and satellite microwave observations (AMSR-E; NCDC 2015) for the years 2002–11. The blending of infrared and microwave data ensures that SST estimates are also available in the presence of clouds. The data were objectively mapped onto a 0.25° × 0.25° global grid at a daily resolution as described in Reynolds et al. (2007).

g. Bathymetry

The bathymetry depicted in this study is from the International Bathymetric Chart of the Arctic Ocean (IBCAO) in its version 3.0 (Jakobsson et al. 2012) that has a 500-m horizontal resolution. In the region discussed in this study, the IBCAO grid is mostly based on multibeam data (IBCAO 2015).

h. Computation of the seasonal cycle

Since this study aims to determine the seasonal cycle of properties and processes in the WSC, different years are not considered individually. Instead, all data with positive quality flags that fall into any January are used to compute the average January value. The same is then done for all months. Given the lengths of the data records that are 5 yr or longer in most cases considered here, small differences in the amount of data used per individual year do not bias the estimates.

3. Seasonality of WSC hydrography and velocity

The monthly averaged data document a considerable seasonality of the structure of the WSC. In winter, the flow has a distinct mean northward component from the shelf edge at 9°E down to the foot of the continental slope at 6°E, with the mean flow being strongest at the shelf edge (Fig. 2a). Conversely, in summer the WSC is well developed over the entire upper slope, but there is very little flow on the offshore side (Fig. 2b). This implies a seasonal lateral shift of the maximum horizontal shear; in winter the strongest decrease in northward flow is on the upper shelf, while in winter it is farther west located on the lower slope. There is significant variability both in the WSC and in the recirculation in

---

[1] Globally Argo data are collected and made freely available by the International Argo Project and the national programs that contribute to it (http://www.argo.net).

[2] Cryosat also covers these latitudes, but no established processing protocol to obtain SSH from the data in ice-free regions exists at this time and the time series would be too short to obtain robust seasonal signals.
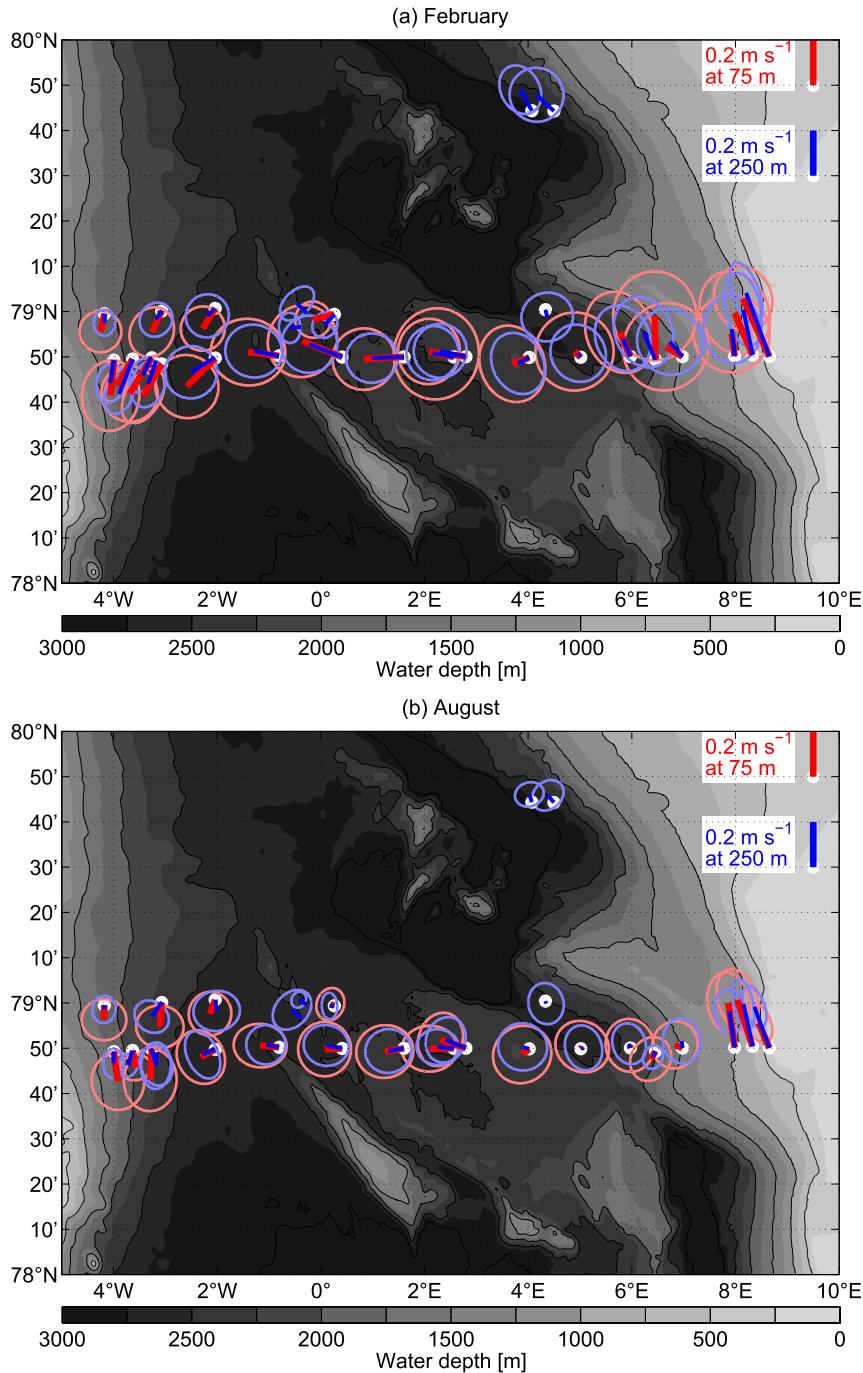
FIG. 2. Mean velocity (m s^{-1}) and standard deviation ellipses from moored instruments in the upper water column. (a) The February mean and (b) August mean. The mooring positions are shown as thick white dots. The monthly mean currents at 75-m depth are shown as thick red lines pointing away from the mooring location. At 250 m, the lines are thinner and blue. The standard deviation ellipses around the mean are shown in light red (75 m) and light blue (250 m). This means that the instantaneous current vectors are inside of the standard deviation ellipses approximately 67% of the time. Scale bars of 0.2 m s^{-1} northward velocity are shown in the top-right corner. These statistics are based on 2-day low-pass filtered data. Individual moorings from different years that are less than 2 nautical miles apart are plotted at the same location in order to reduce the business of the figure while still maintaining a spatial view of the flow. In some deployment years, F4 and F5 (between 6° and 8°E) as well as the moorings in the EGC (F11–F14) were located more than 2 nautical miles from their average location, and therefore they are plotted as multiple current vectors and ellipses here.
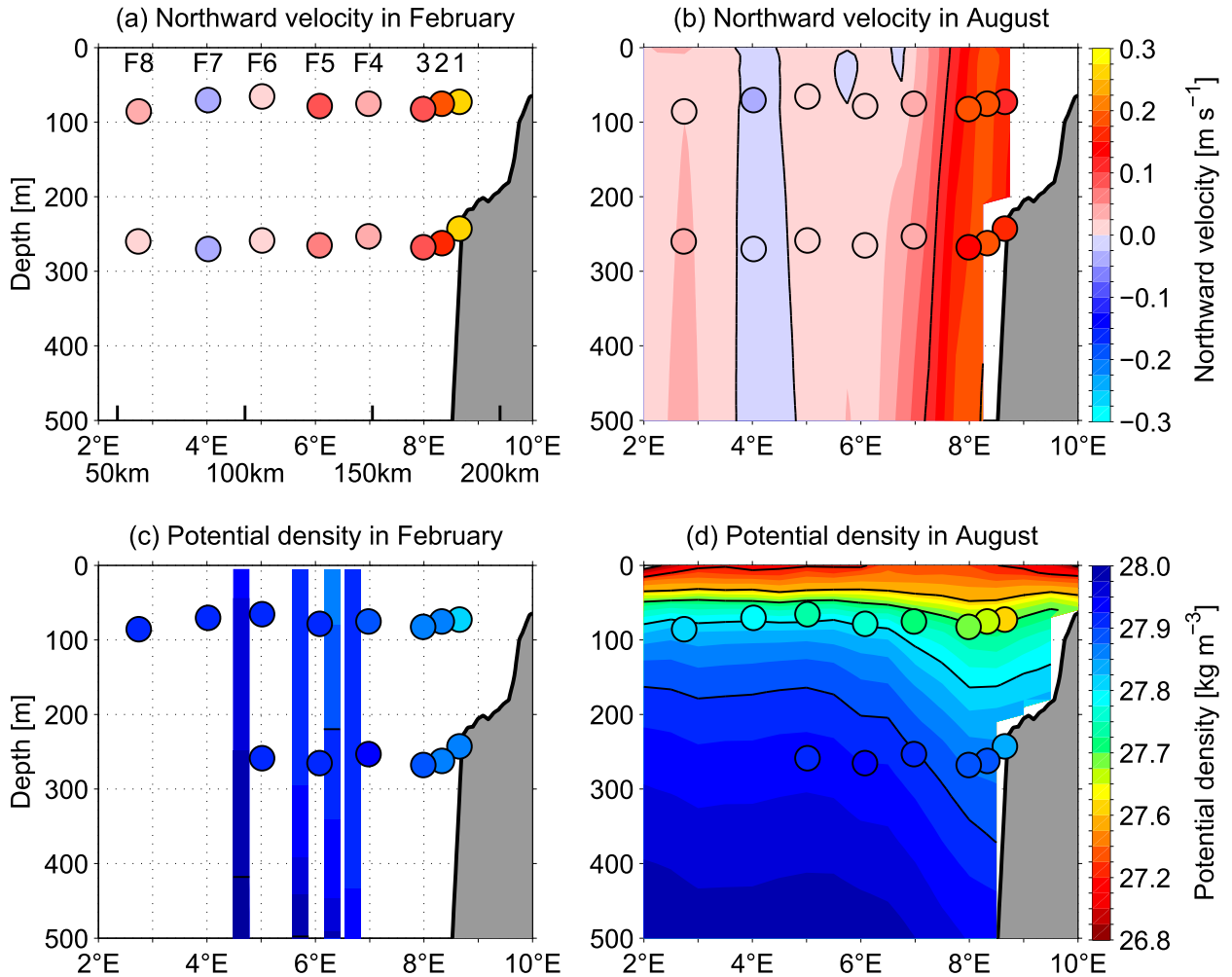
FIG. 3. (a),(b) Northward velocity (m s^{-1}) and (c),(d) potential density (kg m^{-3}) in the WSC (left) in February and (right) in August. The mooring measurements are shown as colored dots at their average locations. The gridded mean potential density of the 16 annual repeat summer (ranging from 20 Jun to 2 Oct) CTD sections (1997–2012) is shown in color in (d). Note the coarser contour resolution below 27.6 kg m^{-3}. Absolute geostrophic velocity calculated using thermal wind from the CTD density field in (d) and referenced to the mooring velocities in (b) is shown in color in (b). Potential density profiles from Argo floats during winter (ranging from 19 Feb to 11 Mar) are shown in color in (c). The typical horizontal spacing of the CTD sections is 7 km [$\approx\frac{1}{3}(1°)$ longitude], and many years have a higher resolution. The bathymetry is indicated in gray. The mooring names and the distance from 0°E are given in (a).

the center of Fram Strait ($\approx$2°W–4°E) in all seasons, but the recirculating flow is a little stronger in winter than in summer (Fig. 2).

The shelf break is located at 230-m depth above the steep slope of West Spitsbergen. As in many locations on earth, also in Fram Strait, the hydrography above 250 m undergoes a significant seasonal cycle, as does the density stratification. While there is not much change at $\approx$250-m depth, the densities above strongly decrease in summer (Fig. 3) with the strongest decrease close to the shelf break. The mooring values in summer agree very well with the average values at those depth horizons from the summer CTD sections occupied between late June and September (Fig. 3a).

The CTD sections show that even lower densities exist in summer above the top mooring instrument horizon. These low surface densities in summer are mostly due to water with reduced salinities (Fig. 4d) that may originate from sea ice melt and filaments of polar water advected from the Arctic Ocean or from the Svalbard coastal current. Below $\approx$50 m, the density decrease and thus the stratification is mostly due to the warming of the AW from spring to summer (Fig. 4b). The six Argo profiles during February and March (Fig. 3c) are among the only winter hydrographic profiles in this region. They show that the water column is very weakly stratified in winter. So the general situation in the WSC is high stratification in summer and weak
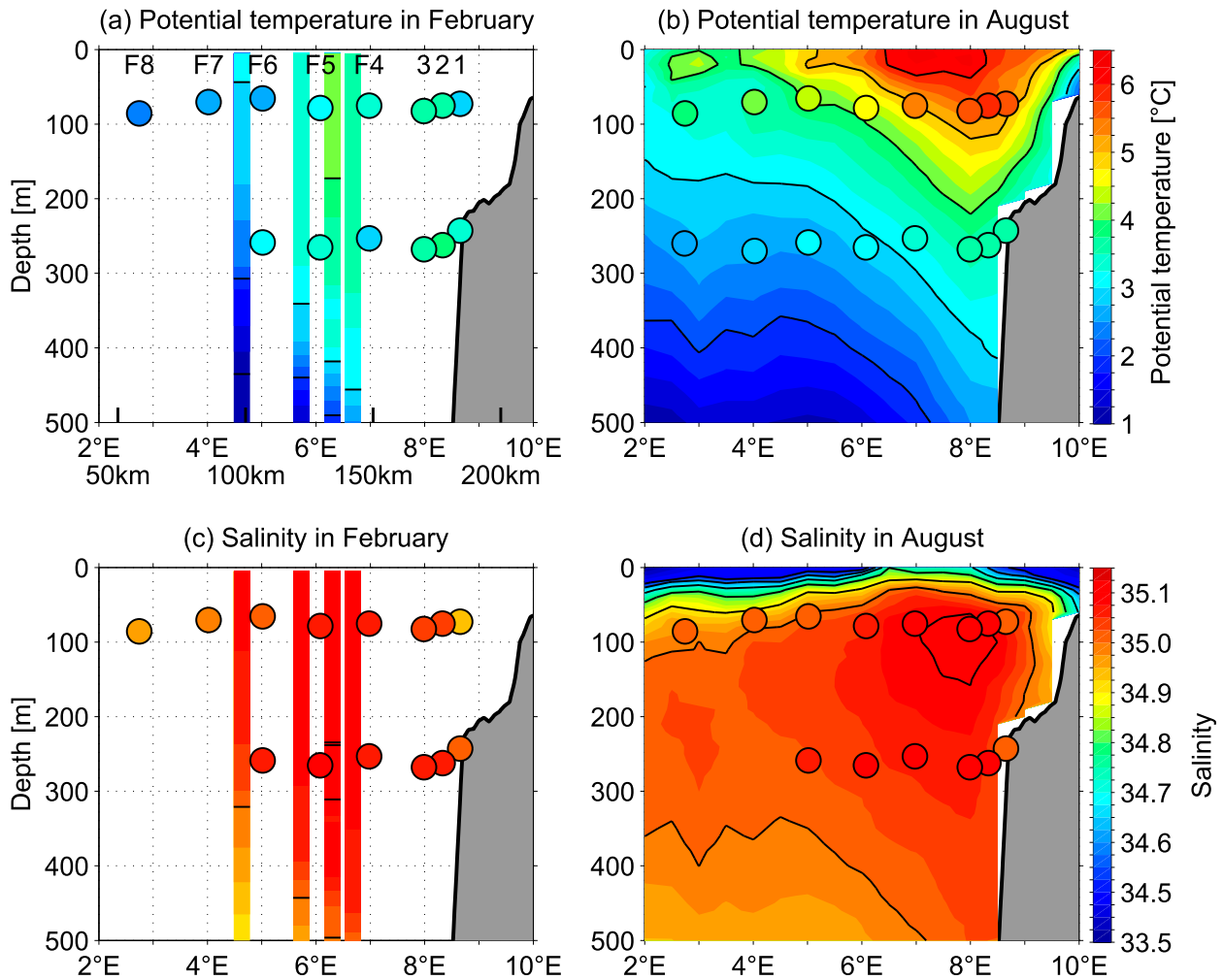
FIG. 4. As in Fig. 3, but for (a),(b) potential temperature (°C) and (c),(d) salinity in the WSC (left) in February and (right) in August. Note the coarser contour resolution below salinities of 34.5.

stratification in winter. Although in summer the core of the WSC is associated with the salinity maximum (Fig. 4d) in ≈100-m depth just offshore of the shelf break, the temperature dominates the density signal and thus leads to the sloping isopycnals (Fig. 3d) and the baroclinic component of the northward boundary current (Fig. 3b).

The mean seasonal cycle of temperature measured from the individual moorings (Fig. 5a) is not symmetric. In 75-m depth, the temperature slowly decreases throughout winter and reaches its minimum in April. In summer, the temperature rapidly rises to its maximum in September. The amplitude of the seasonal cycle in 250-m depth is smaller, and the temperature keeps increasing for longer than higher up in the water column. This means that the seasonal cooling starts earlier higher up than it starts farther down in the water column. In about October the temperatures in the two depth

horizons reach the same values indicating weak vertical gradients resulting in low stratification. The seasonal cycle of the density (Fig. 5c) essentially follows the seasonal cycle of the temperature. Salinity (Fig. 5b) increases in summer, but the density decrease due to the temperature increase is much stronger than the density increase due to salinity.

The sections of northward velocity (Figs. 3a,c) and their seasonal cycle (Fig. 5d) agree with the horizontal view (Fig. 2) discussed above. They highlight that the width of the boundary current is confined to the upper slope (up to F3, ≈8.5°E) in summer. Conversely, the large northward velocities of up to 0.1 m s⁻¹ from November to May at the outer moorings (F4, F5, up to ≈6.5°E) show that the WSC is much wider in winter. With respect to the vertical structure of the northward velocities, the northward velocity on the shelf (F1) is greater in the vicinity of the bottom than at 75 m, while
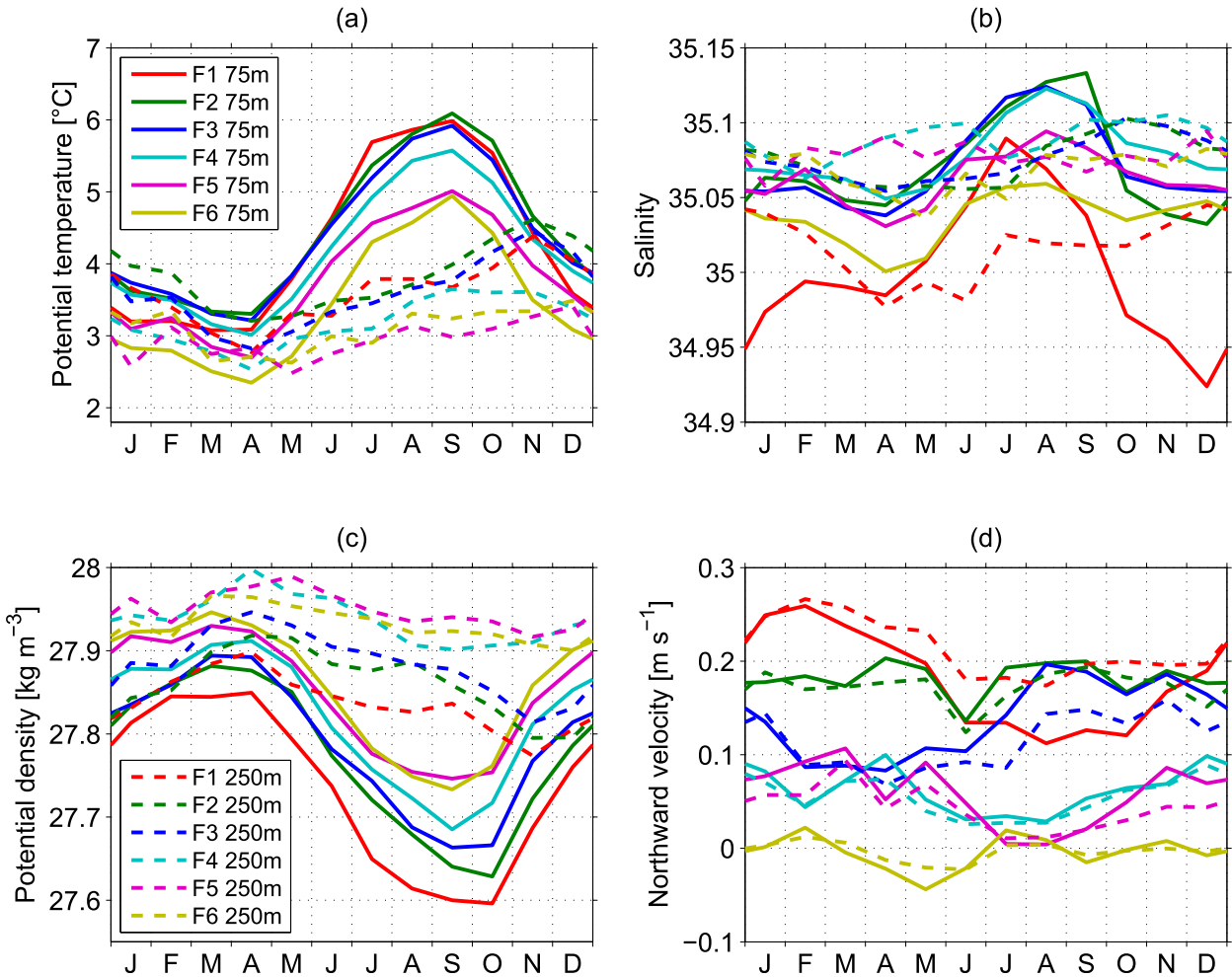
FIG. 5. Seasonal cycle of the hydrography and velocity at 75 m (solid lines) and at 250 m (dashed lines) in the WSC (moorings F1–F6): (a) potential temperature (°C), (b) salinity, (c) potential density (kg m^{-3}), and (d) northward velocity (m s^{-1}). The mooring names are marked in the legends of (a) and (c).

on the slope (F2–F5), the velocity has its maximum in the upper water column and it decreases with depth.

To assess the statistical significance of the above statements, we consider the standard errors of the seasonal cycles discussed above. The standard deviation of the seasonal cycle of temperature is about 2°C at 75-m depth. If a very conservative integral time scale of 10 days for the hydrography is assumed, there are at least three independent estimates per month each year. At the 75-m level, the hydrographic records are at least 7 yr long, which corresponds to about $7 \times 3 = 21$ degrees of freedom and the standard error being $\sqrt{21} \approx 4.5$ times smaller than the standard deviation. Hence, the statistical certainty of our estimates of the seasonal cycle in the upper water column is better than 0.5°C for a seasonal cycle with an amplitude of more than 2°C. Since the standard deviation at the 250-m level is smaller, the

shorter records there (minimum duration of 2 yr) result in standard errors for the temperature of about 0.2°C compared to the seasonal cycle about 1°C. The velocity time series all exceed 12 yr. With typical standard deviations of less than 0.15 m s^{-1} and a seasonal cycle with at least 0.1 m s^{-1} amplitude, the seasonal cycles are statistically well constrained. This means that all the qualitative statements discussed here are statistically significant.

The seasonal cycle of remotely sensed SSH averaged over a 36 km × 84 km box around the moorings (Fig. 6b) has an amplitude of ≈10 cm [as also found by Bulczak et al. (2015)] with the highest sea surface in September. Its shape closely follows the inverse of the density in 75 m. The steric effect of 100 m (typical depth of the warm AW layer) of water changing its density by 0.1 kg m^{-3} (typical summer to winter density difference)
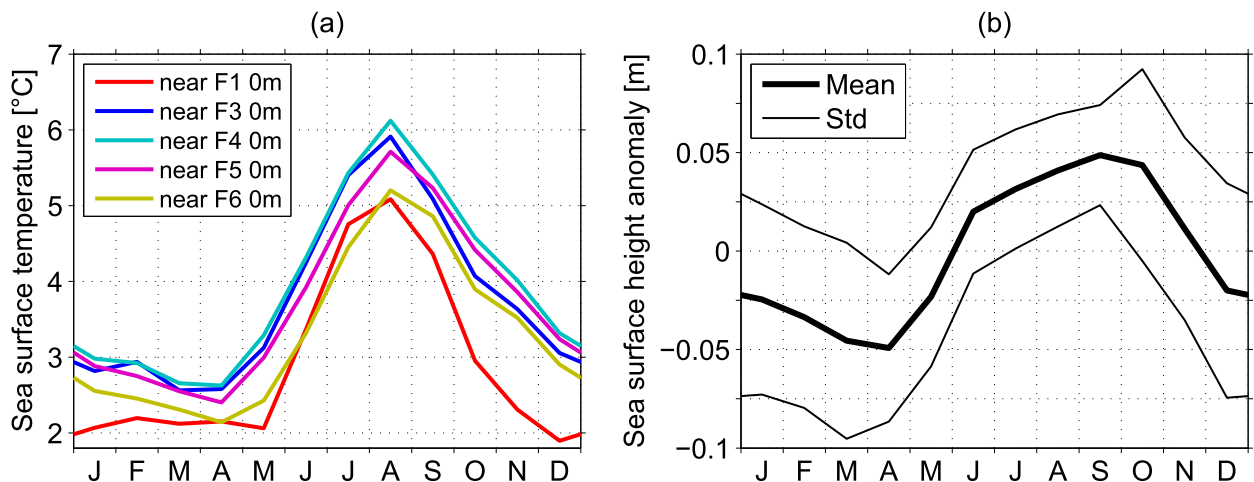
FIG. 6. Seasonal cycle of the satellite-derived (a) sea surface temperature (°C) and (b) sea surface height anomaly (m). The SST is the mean from the AVHRR–AMSR-E blended product within 10 km by 10 km (0.1° latitude by 0.5° longitude) around the mooring locations. The SSH anomaly is the mean from the *Envisat* altimeter within 78°40′–79°N, 5°–9°E, that is, over the WSC and within 18 km latitudinally of the moorings. The anomaly is defined such that the average of the mean curve shown in (b) is zero. The standard deviation of the SSH anomaly is also shown in (b).

corresponds to a SSH change of $100\,\mathrm{m} \times (0.1\,\mathrm{kg\,m^{-3}})/(1025\,\mathrm{kg\,m^{-3}}) \approx 10\,\mathrm{cm}$. Therefore, the SSH seasonal cycle can be attributed to the observed density evolution in the upper water column above the 250-m level (Fig. 5c).

The seasonal cycle of satellite-derived sea surface temperature (Fig. 6a) also agrees well with the seasonal cycle as seen in the moorings (Fig. 5a). However, the surface is colder closer to Svalbard than farther offshore. The winter SST in the western WSC is similar to the respective 75-m temperature but markedly lower (near 2°C rather than 3°C) at F1 on the shelf. The SST peak in summer is narrower and a little bit earlier in the season than that of the 75-m temperature. This confirms the picture emerging from the temperature phase shift between the 75- and 250-m depth levels. The seasonal temperature maxima and minima are reached later in the year at depth. The warming at depth during cooling at the surface (during August to November) suggests that this is an advected signal and is not due to local dynamics.

4. Mesoscale instability diagnostics

In this chapter, we investigate the nature of the current variabilities in the WSC and the recirculation area and their seasonality. The variability is mostly large compared to the mean velocities (Fig. 2). A year-long velocity record at the foot of the continental slope (F6, Fig. 7) where the annual-mean flow is close to 0 (Fig. 5d) shows that the instantaneous eastward and northward velocities can be up to $0.5\,\mathrm{m\,s^{-1}}$. Between early September

and mid-November, the velocities are weak and there is no vertical mooring motion. By contrast, from late December onward, periods with strong currents alternating between northward and southward direction occur. These events may last a couple of days to a week.

a. EKE estimated from the moorings

To quantify the difference between the observed calm and energetic conditions, we compute the EKE in the mesoscale band:

$$\mathrm{EKE} = \frac{1}{2}(u'^2 + v'^2). \quad (1)$$

Here, u' and v' are the eastward and northward velocity components that have been bandpass filtered between 2 and 30 days to focus on the mesoscale band. With the short period limit of 2 days, tides and inertial oscillations are removed, while the long period limit of 30 days removes the seasonal cycle and interannual variations.

In Fram Strait, the largest upper water column variability (EKE $\approx 200\,\mathrm{cm^2\,s^{-2}}$) is observed in the WSC in winter (Fig. 8a), whereas in summer the current is much less variable (EKE $\approx 50\,\mathrm{cm^2\,s^{-2}}$). These values are much larger than the $20\,\mathrm{cm^2\,s^{-2}}$ that can be inferred from geostrophic velocities from summertime CTD surveys (Walczowski and Piechura 2007; Schauer et al. 2008). The maximum of the EKE occurs on the upper slope (F3) in January and is later found farther offshore (maximum at F7 in March). Finally, the maximum variability in the recirculation area of mean westward velocities in central Fram Strait (Fig. 2) is reached still a
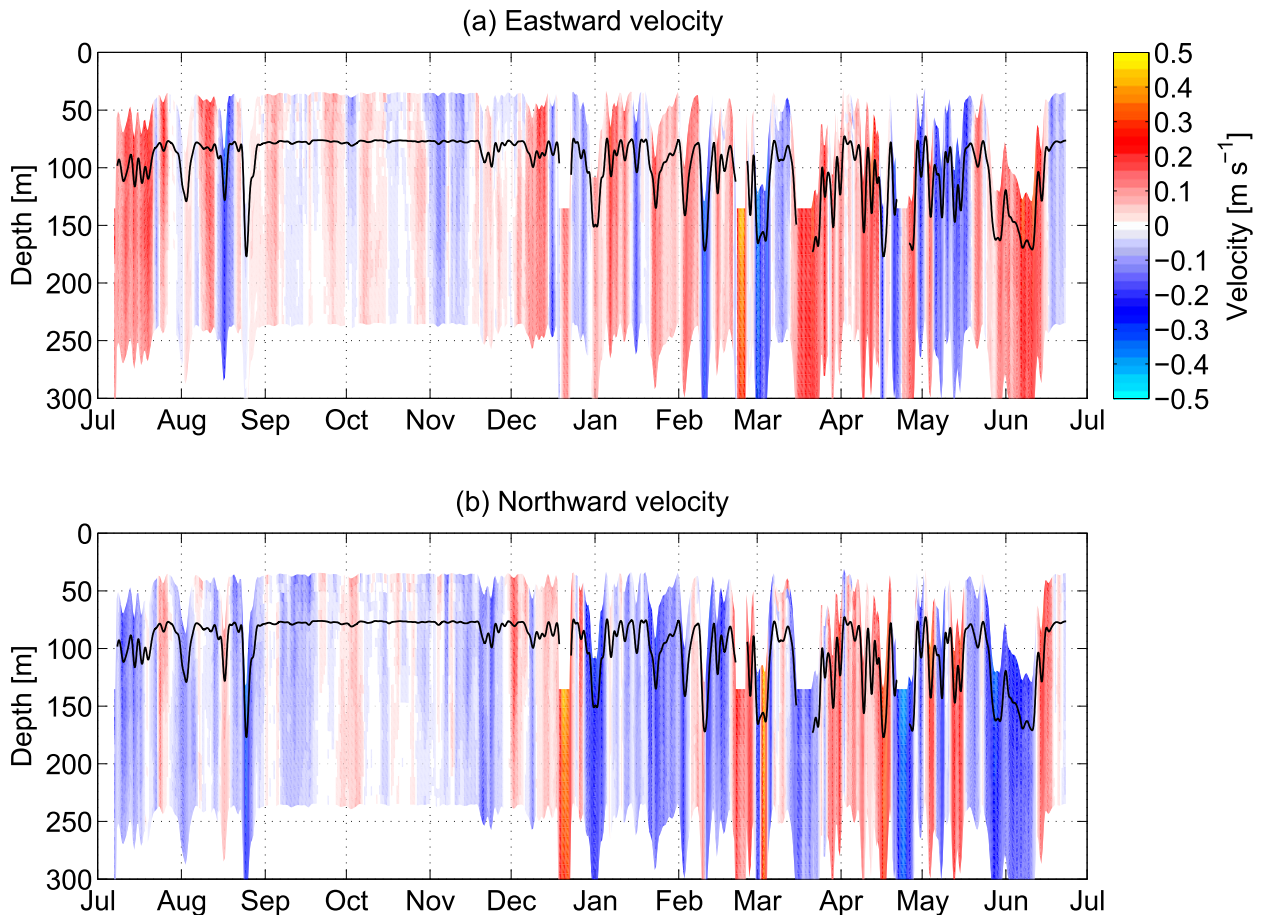
(a) Eastward velocity

(b) Northward velocity

FIG. 7. Example time series of a velocity record. (a) The eastward and (b) the northward velocity (m s^{-1}) at F6 as measured by an upward-looking ADCP at 240-m depth in 2011/12. The velocity has been 2-day low-pass filtered. The black line indicates the depth of a Microcat in the water indicative of the vertical mooring motion resulting from strong horizontal water velocities. This record is used to assign the velocity measurements to the correct water depth. Since the mean velocity at F6 is ≈0 (cf. Fig. 2), the shown velocities are entirely due to the variable flow component.

little later than in the WSC (maximum at F8–F9 in April).

The mesoscale EKE at 75-m depth (Fig. 8a) and at the next instrument level below (250 m; Fig. 8b) is highly correlated ($0.65 < r < 0.95$ and $p < 0.01$ for the different moorings and months). The average ratio in the WSC of the amplitudes at 75 and 250 m for each mooring and each month is 1.7. This points to the fact that the EKE has a baroclinic structure with faster variable motions higher up in the water column, as expected for baroclinic eddies.

The EKE on the shelf (F1) is much weaker (EKE < 70 cm^2 s^{-2}) than on the slope, suggesting that the fluctuations are not generated on and do not move onto the shelf, rather they move offshore. Moreover, it is interesting that the East Greenland Current, captured by F10–F12 (de Steur et al. 2009), is relatively stable as compared to the WSC. The wind forcing on the two sides of Fram Strait is similar (Jónsson et al. 1992). While the

details of the stress transfer from the atmosphere to the ocean might be modified by the mobile sea ice in the EGC compared to the WSC, the integrated forcing of the ocean will still be similar. Thus, if the EKE in Fram Strait was mostly generated by the wind forcing, the EKE level should be comparable in the WSC and the EGC. If instead, the boundary current dynamics are responsible, fundamental differences in the boundary current stability could explain the significant difference in the EKE levels observed in the WSC and the EGC (Fig. 8). This supports an earlier finding (Jónsson et al. 1992) that the EKE in the EGC is very weak and can be sufficiently accounted for by the advection of eddies westward across Fram Strait.

A hypothesis based on this temporal and spatial progression of EKE is that the boundary current is unstable and generates eddies that then move toward the center of Fram Strait (Schauer et al. 2004). This hypothesis
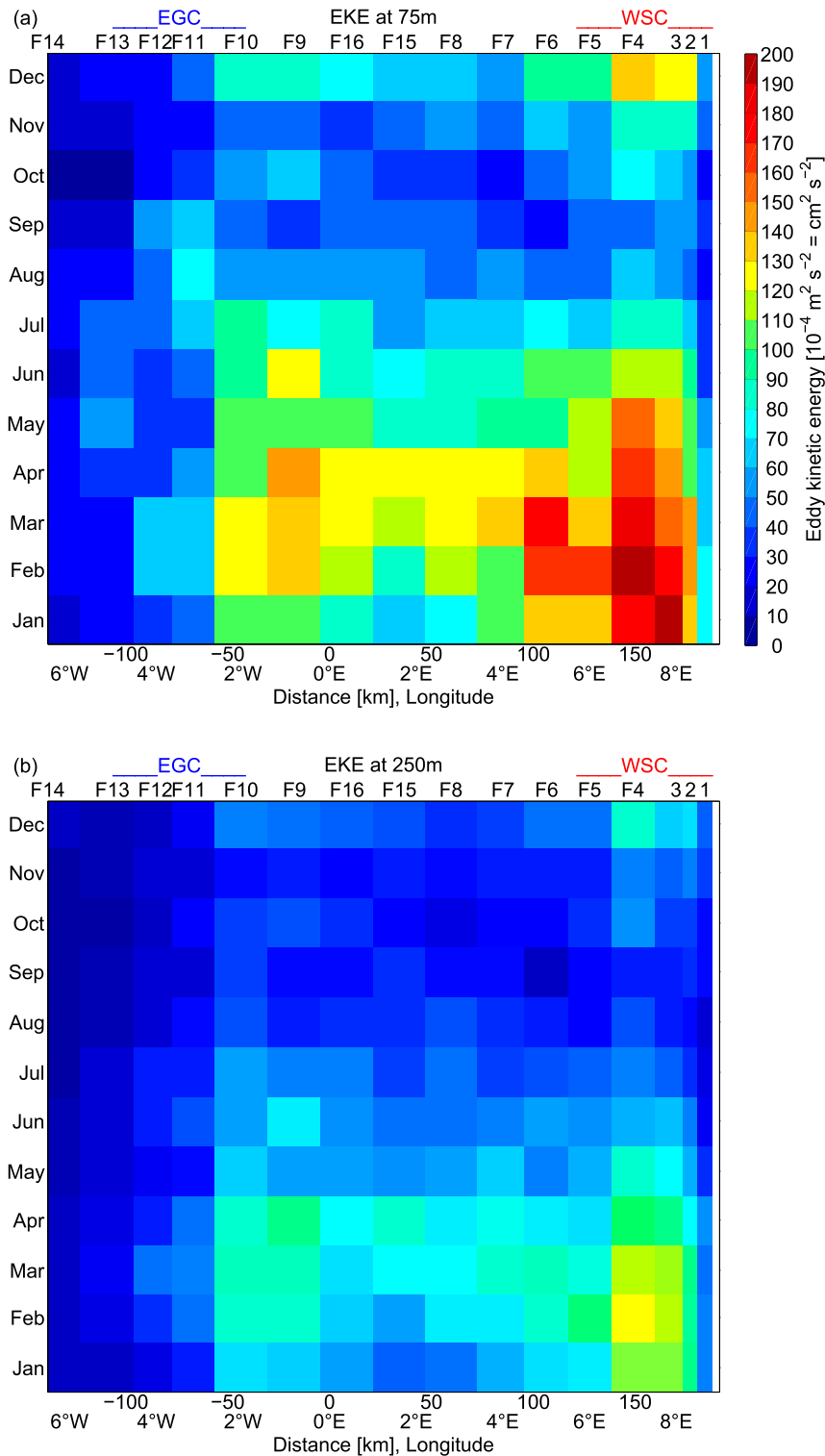
FIG. 8. Seasonal cycle of the eddy kinetic energy ($10^{-4}\,\mathrm{m}^2\,\mathrm{s}^{-2} = 1\,\mathrm{cm}^2\,\mathrm{s}^{-2}$) at (a) 75-m depth and (b) 250-m depth as a function of zonal distance across Fram Strait. The approximate locations of the West Spitsbergen Current and the East Greenland Current are marked at the top. The EKE is defined as $(1/2)(u'^2 + v'^2)$, where u' and v' are the bandpass-filtered velocities with cutoff periods of 2 and 30 days as measured from the moorings. Note that the seasonal progression at 250 m is similar to the progression at 75 m, but with a reduced amplitude (averaged over F1–F6 and all seasons): EKE(75 m) $\approx$ 1.7 $\times$ EKE(250 m). The progression at the deeper depths (750 and 1500 m) is also similar but with further reduced amplitudes ($< 40 \times 10^{-4}\,\mathrm{m}^2\,\mathrm{s}^{-2}$).

implicitly assumes that the eddy field is advected by some background current or is self-advecting. Indeed, in such a situation when an eddy moves past a mooring, the mooring will experience the variability associated with the eddy. In the opposite case of an eddy that is stationary, that eddy would be associated with a constant velocity and hence no variability (EKE = 0) at a fixed point. However, there are northward velocities in the eastern and westward velocities in the central Fram Strait (Fig. 2). Hence, the background flow can advect the eddies past the measurement location, supporting the assumption that the EKE is not due to stationary eddies. With our method of diagnosing EKE, we cannot distinguish between a meandering current that is a small-amplitude linear disturbance and a fully developed eddy that may develop from the small-amplitude case as the amplitudes grows. Still both features are consistent with the above hypothesis as they represent different stages of the eddy generation mechanism. Other explanations for the enhanced EKE values in the central Fram Strait could be that the recirculation branch near the mooring line may itself be subject to instabilities or may be meandering over the moorings and then away seasonally. Furthermore, frontal processes at the ice edge and/or the region where Polar Water comes into contact with Atlantic Water may lead to variability.

b. EKE estimated from along-track satellite altimetry

To complement the mooring-based estimates of EKE that are only available along 78°50′N, we now consider regionwide EKE estimates derived from satellite altimetry. Gridded SSH data products provide valuable information about eddies in lower latitudes where the Rossby radius is much larger than in Fram Strait, and the associated time scales of the eddies are closer to the typical averaging period for the gridding of more than a week. To avoid the smoothing of small eddies expected in the high-latitude (large Coriolis parameter) Fram Strait, we use along-track sea surface height $\eta(x, y, t)$. Subtracting the time average $\overline{\eta}(x, y)$ at each point of the repeating orbits yields the sea surface height anomaly $\eta'(x, y, t)$. The gradient of η' in the along-track direction x yields the surface geostrophic velocity v'_g in the cross-track direction y:

$$v'_g = \frac{g}{f} \frac{\partial \eta'}{\partial x}. \tag{2}$$

Since along-track data can only detect the surface geostrophic velocity in the cross-track direction, isotropy is assumed when estimating EKE from along-track data (e.g., Lilly et al. 2003). That is, it is assumed that the variable part of the flow in the along-track direction and

the cross-track direction have roughly the same amplitude, which is reasonable for an eddy field. The term u' is then substituted by v'_g in Eq. (1) to result in EKE = $(1/2)(v'^2_g + v'^2_g) = v'^2_g$. For the ice-free regions, monthly averages of v'^2_g in 21-km zonal width by 18-km meridional width bins were calculated for the satellite period (2002–12).

In winter (Fig. 9a), an elongated band of high EKE of between 100 and 200 cm^2 s^{-2} is located over the lower continental slope along the pathway of the offshore WSC branch. Farther offshore in the Greenland Sea Gyre (≈4°E and south of 78°N), the variability is very weak. As a result, there is a strong EKE gradient between the quiet Greenland Sea Gyre and the energetic boundary current. However, the zonal gradient is less steep near and south of 79°N, which is also where the moorings are located. The westward flow of the recirculation there likely advects EKE across Fram Strait. In summer (Fig. 9b), the situation is quite different. Consistent with the seasonal cycle from the moorings (Fig. 8), the amplitudes throughout are much weaker in summer than in winter. The band of large fluctuations associated with the offshore side of the boundary current in winter is mostly absent; there is only a little bit of variability on the slope north of 78°N.

Since we average over all Februaries (Fig. 9a), individual eddies are not discernible, yet the EKE distribution features isolated maxima. This is consistent with the dynamics of a boundary current passing regions where the topography leads to stronger instability than in others. Alternatively, we note that these features could also be due to aliasing of the fields computed from the polar orbiting satellites (Zeng and Levy 1995).

The monthly means of EKE from the moored instruments in 75 m (Fig. 8) agree well with the surface geostrophic EKE from the satellite altimetry (Fig. 9). Consistently between the two datasets, on the shelf, the amplitudes are weak, and on the slope, the amplitudes are quite high and they then decrease a little bit toward the center of Fram Strait. The three Hausgarten moorings were located to the north and south, but they only had current measurements at 250 m, so the average EKE ratio of 1.7 between 75 and 250 m from the other moorings (Fig. 8) was used to upscale the EKE estimated from the Hausgarten moorings at 250 m. Then the amplitudes are consistent suggesting that the different data sampled the same features. This comparison between the mooring EKE and the SSH EKE is actually based on the 2- to 30-day bandpass-filtered velocities and the sea surface height that has an intrinsic resolution of 10 km. This is because in the along-track direction only one independent SSH estimate is achieved every 10 km, which intrinsically smooths all processes on
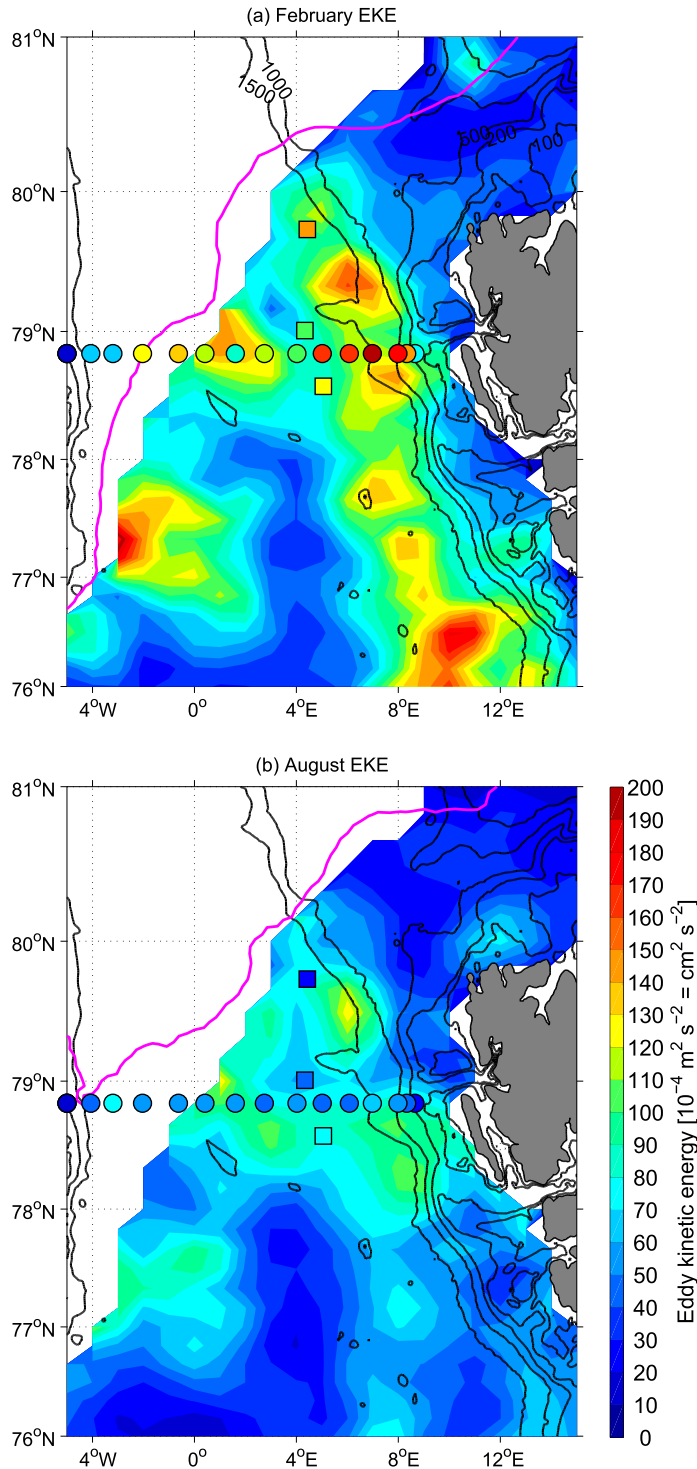
FIG. 9. Eddy kinetic energy ($10^{-4}\,\mathrm{m^2\,s^{-2}} = 1\,\mathrm{cm^2\,s^{-2}}$] in (a) February and (b) August as determined from the along-track sea surface height anomalies of the *Envisat* altimeter. See section 4b for the calculation of the EKE. The EKE in 75-m depth from the moorings (cf. Fig. 8a) along 78°50′N is shown as filled colored circles. The EKE in 250 m from the Hausgarten moorings was upscaled by 1.7 to its presumed values at 75 m and is shown as filled colored squares. The mean ice edge (defined as the 50% ice concentration line) in (a) February and (b) August from the AMSR-E/AMSR-2 microwave sensor is shown in magenta. The isobaths are labeled in (a).

distance scales smaller than 10 km. Here, we picked a particular range of spatial scales for the satellite data and a different particular range of temporal scales for the moorings, but both the amplitudes and their qualitative distribution in space and time agree very well. We conclude that the EKE resolved here only exists in the temporal and spatial band of mesoscale dynamics and is therefore due to mesoscale motions. In summary, we have established that the boundary current along the slope is associated with elevated EKE, especially in winter. South of 78°N, the EKE associated with the eddies does not leave the boundary current.

We also note that our EKE estimate differs from a previous estimate of EKE based on satellite altimetry spanning both ice-free and ice-covered areas (Bulczak et al. 2015). In that study, isotropy was not assumed to calculate EKE but instead the sea surface height anomalies were first mapped with a Gaussian weighting function with a horizontal half-width of 60 km. The resulting space and time smoothing is greater than for the isotropy assuming method (Lilly et al. 2003) used here. Therefore, we find higher values of the EKE in the WSC in both summer and winter than Bulczak et al. (2015) did. Conversely, during November–January, the moorings indicate much smaller EKE values in the EGC ($\approx 20\,\mathrm{cm^2\,s^{-2}}$) and near the ice edge ($\approx 100\,\mathrm{cm^2\,s^{-2}}$) than what was determined from satellite altimetry in the EGC ($\approx 100\,\mathrm{cm^2\,s^{-2}}$) and near the ice edge ($\approx 200\,\mathrm{cm^2\,s^{-2}}$) by Bulczak et al. (2015). Bulczak et al. (2015) attributed the ice edge amplification of EKE to oceanic jet formation resulting from the change in surface roughness as local winds transition to/from the ice/ocean (e.g., Heorton et al. 2014). We note that our observations do not and cannot distinguish between eddies caused by wind from those generated by instabilities.

c. Energy conversions estimated from the moorings

We now estimate the energy conversion rates in the WSC associated with mesoscale instabilities that can form mesoscale eddies and contribute to the weakening of the boundary current. A general concept of baroclinic instability is to transfer mean available potential energy to eddy energy with the baroclinic mean-to-eddy conversion BC defined as (Spall et al. 2008)

$$\mathrm{BC} = g\gamma\overline{u'\rho'}. \qquad (3)$$

Likewise, barotropic instability transfers mean kinetic energy to eddy energy and the barotropic mean-to-eddy conversion BT is defined as

$$\mathrm{BT} = \rho_0\overline{u'v'}\frac{\partial\overline{v}}{\partial x}. \qquad (4)$$
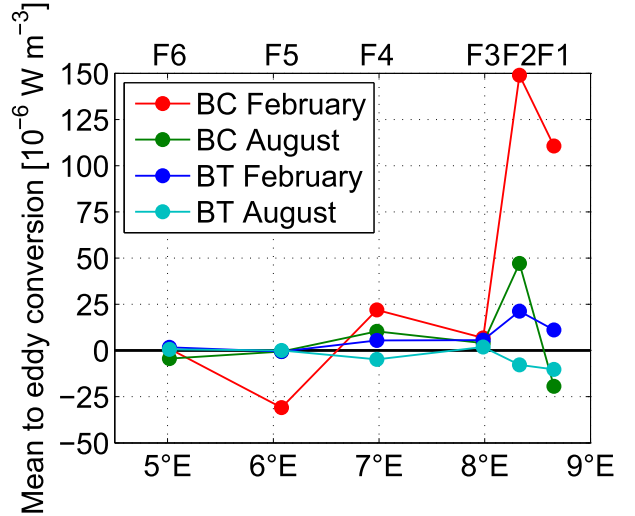

FIG. 10. Baroclinic and barotropic conversion ($10^{-6}\,\mathrm{W\,m^{-3}}$) from mean-to-eddy energy in the WSC in February and in August at a depth of approximately 75 m. The shelf break is at 8.5°E. Baroclinic conversion is the transfer from mean available potential energy to eddy energy. Barotropic conversion is the transfer from mean kinetic energy to eddy energy. See section 4c for how the conversions were defined and calculated.

Here, y is the along-stream direction that in our case is roughly northward, and x is the onshore direction that in our case is roughly eastward. The terms u and v are the velocity components in the x and y directions, respectively. Furthermore, g is the gravitational acceleration, ρ is the density, and $\gamma = -\partial z/\partial x = (\partial\overline{\rho}/\partial x)/(\partial\overline{\rho}/\partial z)$ is the mean slope of the isopycnals in the onshore direction. The overbar corresponds to temporal averaging, and the primes are the deviations from the mean due to the variable part of the flow. The conversions were calculated from the moored instruments in 75 m; the difference between the 75- and 250-m data was used to estimate the vertical gradients. Since the mooring spacing is similar to or larger than the Rossby radius (cf. section 5b below), the horizontal gradients are likely underestimated. As a result, the exact amplitude of the estimates from the moorings (Fig. 10) may be incorrect, but the qualitative structure that emerges is nonetheless informative with respect to the ratios of the conversions between the different cases.

The baroclinic conversion in winter (Fig. 10) is strongly positive on the upper slope. Also in summer it is mostly positive in the boundary current, but the amplitude is much smaller and there is a region of negative conversion on the shelf. The barotropic conversion in winter is positive, but its amplitude is comparable to the baroclinic conversion in summer. Finally, the barotropic conversion in summer is slightly negative. The conversions follow the seasonal pattern (not shown) with February and August representing extreme cases.
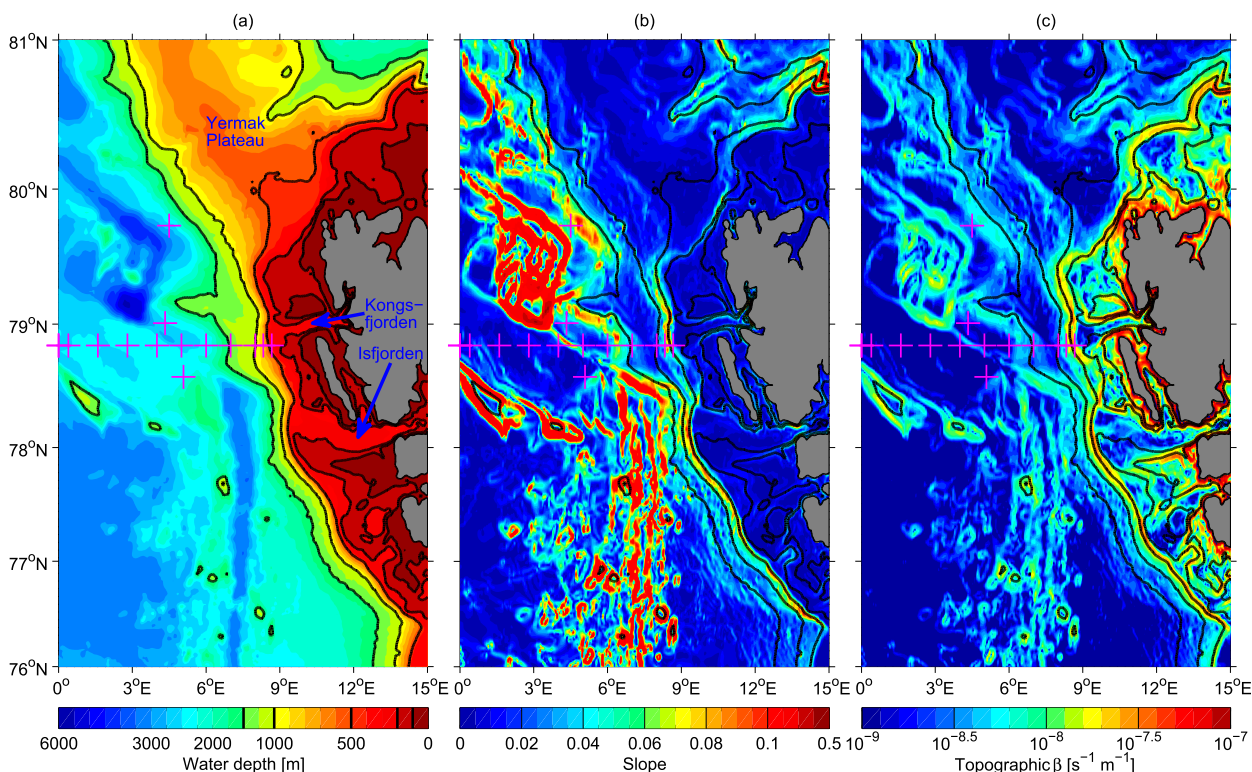
FIG. 11. Topography along the West Spitsbergen margin from IBCAO V3.0. (a) Water depth (m), (b) slope, and (c) the topographic $\beta = -(f/H)\nabla_h H\,(\mathrm{s}^{-1}\,\mathrm{m}^{-1}$; plotted logarithmically). The bathymetry was smoothed over about 5 km by 5 km for calculating (b) and (c). The mooring locations are shown as magenta $+$ and land is gray.

Altogether, these energy conversion rates indicate that the WSC is strongly baroclinically unstable in winter and a little less so in summer. Barotropic instability also seems to play a role in winter but appears to be absent in summer.

5. Mesoscale instability prognostics

a. Barotropic instability

Can we assess the conditions when barotropic instability occurs? From a conceptual point of view, strong horizontal velocity gradients support barotropic instability, whereas steep bathymetry can suppress barotropic instability. The change in background potential vorticity across the bathymetry is quantified by the topographic $\beta = -(f/H)\nabla_h H$. Here, f is the Coriolis parameter, H is the water depth, and ∇_h is the horizontal gradient. The topographic β therefore has a similar effect as the planetary β that quantifies gradients in the background planetary vorticity associated with the latitudinal extent of motions and is very small for motions from 75° to 80°N ($\beta \approx 5 \times 10^{-12}\,\mathrm{s}^{-1}\,\mathrm{m}^{-1}$). The topographic β (Fig. 11c) was estimated from the water depth

(Fig. 11a) and the bottom slope (Fig. 11b). All along the West Spitsbergen shelf break between 76°20′ and 79°30′N, β is large ($\approx 2 \times 10^{-8}\,\mathrm{s}^{-1}\,\mathrm{m}^{-1}$), but a small reduction is seen south of the mooring array between Isfjorden and Kongsfjorden.

A necessary condition for barotropic instability is that $\beta - (\partial^2 v/\partial x^2)$ changes sign somewhere in the domain (e.g., Vallis 2006). Here, v is the along-stream velocity of the current and x is its typical cross-stream width. The condition can only be fulfilled if β and v_{xx} have the same order of magnitude somewhere in the domain. The typical width of the WSC is $x \approx 5$ km, and the flow speed decays from the maximum of $v \approx 0.25\,\mathrm{m\,s}^{-1}$ in the center of the boundary current to ≈ 0 over this scale x. Hence, v_{xx} has a typical magnitude of $1 \times 10^{-8}\,\mathrm{s}^{-1}\,\mathrm{m}^{-1}$. The maximum value of β in the cross-stream direction exceeds these estimates along most of the shelf break south of 79°20′N (where the Yermak Plateau starts). However, over the $\approx 20′$ latitudinal extent just south of the mooring array, β is smaller and the necessary condition for barotropic instability may be fulfilled when the boundary current is fast and narrow.

The necessary condition for barotropic instability can also be fulfilled if v_{xx} increases. The velocity at the most

inshore mooring is smaller in winter than in summer (Figs. 2, 5d). Hence, the width of the nonsymmetric current on the onshore side is smaller in winter. So we conclude that the condition for barotropic instability might be fulfilled in winter in the region just south of the mooring array but that elsewhere along the West Spitsbergen slope and at other seasons, the current is likely barotropically stable. This is consistent with the 60% barotropically stable times seen by Teigen et al. (2010) at the latitude of the mooring array.

Since the topographic β is very small along the continental slope of the Yermak Plateau north of 79°20′N, the dynamics of the boundary current over the Yermak Plateau are likely very different than along the West Spitsbergen margin south of 79°20′N. On the Yermak Plateau, on the other hand, the bathymetry does not stabilize the boundary current and the necessary condition for barotropic instability is very likely fulfilled. This presumably contributes to the eddying northern recirculation branch there (Hattermann et al. 2016, manuscript submitted to *Geophys. Res. Lett.*). On the other hand, Lagrangian floats ballasted to about 300-m depth have been found to travel northward along the Yermak Plateau to about 80°40′N and to then turn eastward into the Arctic Ocean (Gascard et al. 1995), suggestive of the fact that the boundary current there may not, in fact, completely disintegrate.

So, consistent with the energy conversions (Fig. 10), we found that in winter barotropic instability may contribute to the growth of the eddies that are observed as the variability at the mooring array (Fig. 8).

b. Baroclinic instability

Baroclinic instability can generate eddies, and parameterizations exist that quantify how much EKE may be generated by the instability. EKE has units of distance squared over time squared. On dimensional grounds, the square of the background velocity may scale as EKE [parameterization of Stone (1970)]. Likewise, the Rossby radius may be considered as a distance scale, and the inverse of the *e*-folding growth rate of the instability may be considered as a time scale. The square of the product of these may then scale as EKE [parameterization of Killworth (1997)]. With the combination of mooring data and high vertical resolution ship and Argo CTD profiles, we have the necessary datasets to estimate these parameters. First, we estimate the stratification and the shear. The growth rate is then estimated from stratification and shear while the Rossby radius only depends on stratification. Finally, we evaluate the level of EKE that baroclinic instability can generate in the WSC according to the parameterizations.

1) STRATIFICATION

Since the moorings provide measurements only at distinct levels, stratification $N^2 = (-g/\rho_0)(\partial\rho/\partial z)$ cannot exactly be calculated. Yet we consider the density difference between 75 and 250 m as a measure for the upper-ocean stratification[3] in the dynamical depth range of the WSC, and from this we can estimate its temporal evolution (Fig. 12a). In the winter months, the stratification is more or less constant and small but nonzero and then it increases toward summer before decreasing again. On the upper slope, the stratification is somewhat enhanced compared to farther west. The stratification estimated from the mean of the summer CTD stations (Fig. 3) is in good agreement with the mooring data (Fig. 12a). The stratification estimates from the 14 Argo profiles also follow the mean evolution determined from the moorings. But there are also a few cases in winter when the stratification essentially vanishes. These infrequent events are also present in the mooring temperature and salinity time series at the two depth levels (not shown). They are indicative of convection events reaching at least 250-m depth either at or in close horizontal proximity to the moorings. However, the dynamically relevant quantity for baroclinic instability is rather the average stratification in a particular time period that is nonzero also in winter.

2) SHEAR AND RICHARDSON NUMBER

The shear $S^2 = (\partial v/\partial z)^2$ is estimated from the velocity difference between 75 and 250 m. It also has a seasonal cycle. In winter it is a little stronger than in summer (Fig. 12b). The shear only varies by a factor of 2, whereas the stratification changes by a factor of 5. Dividing the two quantities by each other yields the Richardson number $\mathrm{Ri} = N^2/S^2$ that ranges from about 3 in winter to around 30 in summer. This means that both the stratification and the shear contribute to the factor of 10 difference in the Richardson number between the seasons.

3) GROWTH RATE OF BAROCLINIC INSTABILITY

A necessary criterion for baroclinic instability is the reversal of the sign of the horizontal gradient of the total potential vorticity (which scales as the stratification) somewhere in the domain. Given that we only have one estimate (density difference between 75 and 250 m) of N^2 (and hence potential vorticity) per mooring, we

---

[3] Note that stratification is not affected by mooring motion to lowest order since both the nominal 75-m instrument and the nominal 250-m instrument move vertically together.
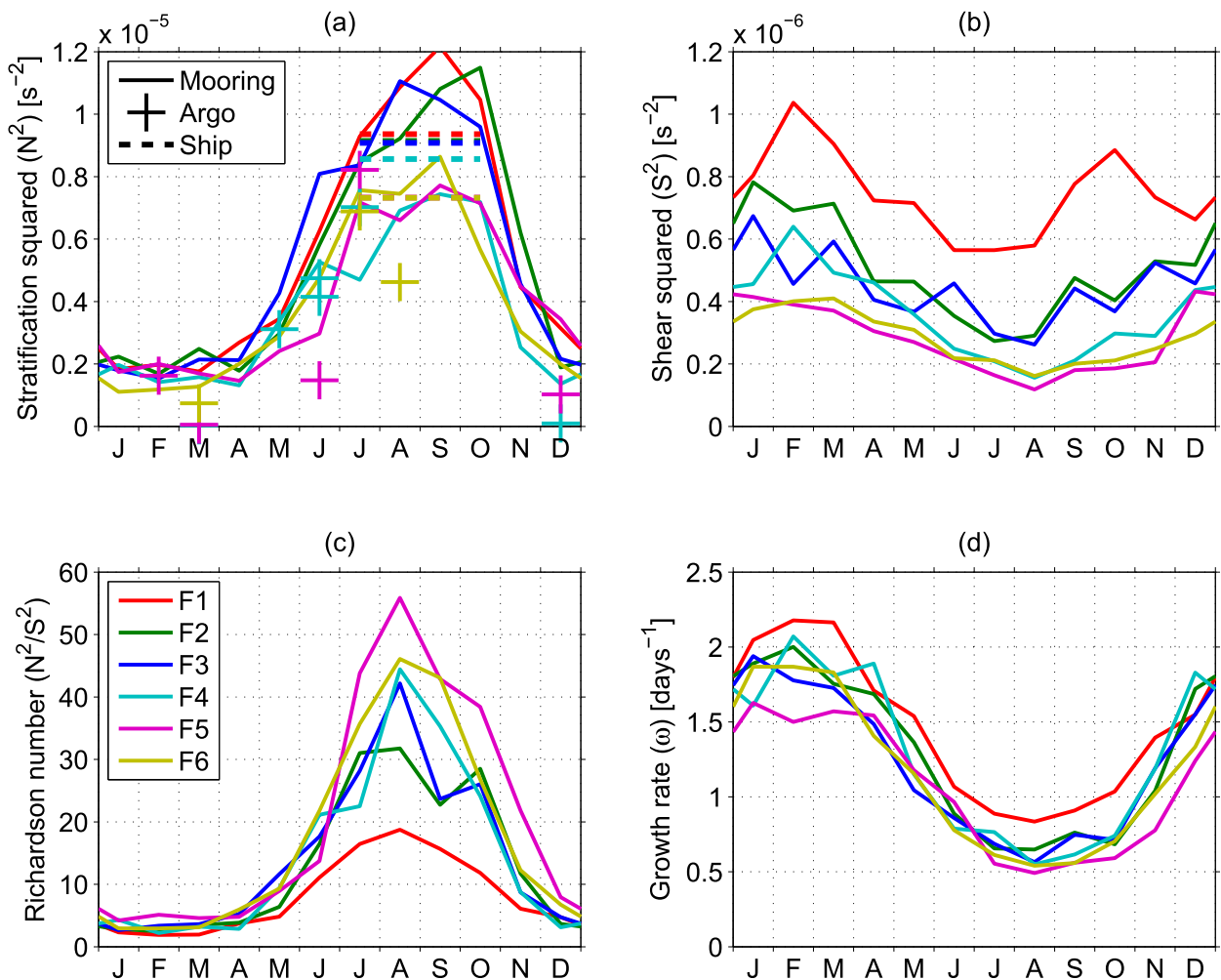
FIG. 12. Seasonal cycle of stability characteristics in the WSC (moorings F1–F6): (a) stratification squared N^2 (s^{-2}), (b) shear squared S^2 (s^{-2}), (c) Richardson number Ri, and (d) growth rate of baroclinic instabilities ω (days^{-1}). The colored solid lines are the monthly averages from the moorings [names are given in (c)]. The + in (a) are from the Argo profiles and the dashed lines in (a) are estimates from the mean CTD section (Fig. 3d) evaluated at the mooring longitudes shown as spanning the typical range of the dates of the section occupations. Note that the range of the shear (b) is only a tenth of the stratification (a).

cannot detect such gradient changes if they occur one over the other in the vertical (which is commonly the case in boundary current systems; e.g., Spall and Pedlosky 2008). However, we can check what the implications for the variability would be if the current was baroclinically unstable. If those implications agree with the observations of the variability, that would support the conclusion that the current is in fact baroclinically unstable.

Conceptually, a relatively strong vertical shear, which in geostrophic conditions is related to a strong horizontal density gradient, supports baroclinic instability. Likewise, a relatively strong vertical stratification suppresses baroclinic instability. The Richardson number Ri expresses the ratio of these two parameters, and small

Ri support baroclinic instability. Eady (1949) derived the e-folding growth rate ω for the baroclinic instability of a two-layer finite-depth flow. Note that the Eady problem deals with linear small-amplitude disturbances that do not feed back on the mean flow. The familiar textbook solution can be rewritten (e.g., Thomsen et al. 2014) using thermal wind to be expressed in terms of the Ri number: $\omega^2 \approx 0.09 f^2/\mathrm{Ri}$. The Eady problem is only valid for large stratification (Ri $\gg$ 1). Since the stratification is weak in winter (Fig. 12c), we consider the following version here. Stone (1970) found that accounting for the effects of weak stratification (Ri $\gtrsim$ 1) leads to a small correction for the e-folding growth rate ω that is then also valid for small Ri: $\omega^2 \approx 0.09 f^2/(1 + \mathrm{Ri})$. We use the estimates of Ri (Fig. 12c) to estimate the growth rate
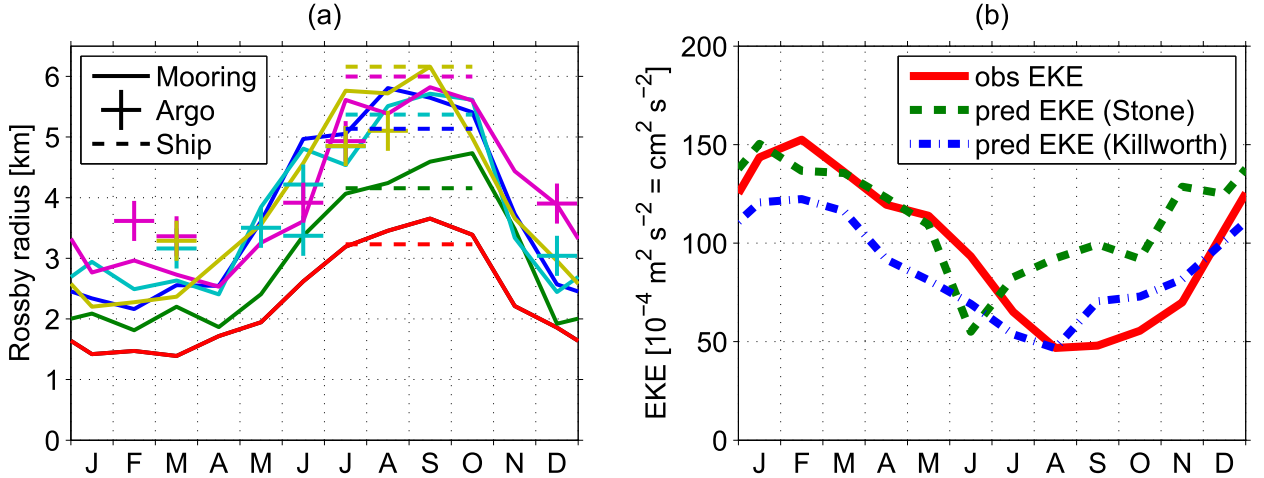
FIG. 13. Seasonal cycle of the (a) Rossby radius (km) and (b) EKE (10^{-4} m^2 s^{-2} = 1 cm^2 s^{-2}) in the WSC (moorings F1–F6). The Argo (+) and the ship (dashed lines) estimates in (a) are evaluated from the full water depth profiles. The mooring estimates use the stratification evaluated between 75 and 250 m and a baroclinic height H of 150 m for F1, 200 m for F2, 250 m for F3, and 300 m for F4–6. The observed EKE in (b) is $(1/2)(u'^2 + v'^2)$ at 75-m depth, the Stone (1970) parameterization is $v'^2 = a\overline{u}^2$ with $a = \frac{1}{2}$, and the Killworth (1997) parameterization is $v'^2 = b\omega^2 R_d^2$ with $b = \frac{1}{4}$. The colors in (a) correspond to the different moorings as in Figs. 5 and 12. The values in (b) are evaluated for each month at each mooring and then averaged zonally over F1–F6.

(Fig. 12d). The variations between the moorings are small and everywhere show growth rates of about 2 day^{-1} in winter and about 0.5 day^{-1} in summer. This shows that if the instability has amplitude 1 at time t_0, it will have grown to an amplitude of $e \approx 2.72$ at time $t_0 +$ 12 h in winter, while it takes about 48 h in summer for that to occur. So the instability grows about 4 times as fast in winter than in summer. These estimates of the growth rate have a similar order of magnitude to what is found in other high-latitude baroclinically unstable boundary currents. For example, the growth rate in the Labrador Current is ≈ 1.5 day^{-1} in winter and ≈ 0.5 day^{-1} in summer (Thomsen et al. 2014). Both the decrease in stratification and the increase in shear act toward destabilizing the WSC in winter, but also in summer the current is not entirely stable.

4) ROSSBY RADIUS

The first baroclinic Rossby radius of deformation R_d is the distance that information can propagate as a baroclinic wave in a pendulum day. In general, it is the solution to an eigenvalue problem, but it can be approximated for a flat bottom as the following integral over the whole water column from the bottom ($z' = z_{\text{bottom}}$) to the surface ($z' = 0$; e.g., Chelton et al. 1998):

$$R_d = \frac{1}{f} \int_{z'=z_{\text{bottom}}}^{z'=0} N(z')\, dz'. \qquad (5)$$

Since the pycnocline occurs in the upper fraction of the water column in the WSC, the modifications to the Rossby radius due to the sloping bottom are likely small and negligible. The approximation of Eq. (5) is good to within about 20% of the exact solution in the Arctic Ocean (Nurser and Bacon 2014). For a constant stratification N over a water depth H, Eq. (5) can be further simplified to $R_d = (NH)/f$.

Using Eq. (5), from the summer ship-based CTD profiles (Fig. 3d), we calculate (Fig. 13a) a Rossby radius of 3–4 km on the shallow (≈ 300 m) West Spitsbergen shelf and 4–6 km in the deeper Fram Strait. The year-round Argo profiles only reach to 2000-m depth (no profiles on the shelf are available). But since, in the vicinity of the deep moorings, the stratification as well as its seasonal variation is small below 2000 m (von Appen et al. 2015b), we just extend the Argo profiles to the bottom using the profiles from the mean CTD section. The summer values of 4–6 km (Fig. 13a) agree well. Then in winter the Rossby radius is small (about 3–4 km) also in the deep Fram Strait. This is because of the eroded stratification in the upper ocean in winter.

The moorings only provide the average stratification between 75 and 250 m (Fig. 12a). If one assumes that the pycnocline is associated with the density contrast between those two depth levels, the Rossby radius would depend on the average stratification. To proceed, we assume a simplified 1.5-layer ocean where the upper ocean of stratification N and depth H accounts for motions, while the underlying unstratified ocean is motionless. We then adjust the baroclinic height H such that the mooring estimate (Fig. 13a) of the Rossby radius $R_d = (NH)/f$ approximately agrees with the

ship-based estimates in summer. On the shelf (F1), the baroclinic height H is 150 m and increases to 300 m in the deep Fram Strait (F4–F6). The resulting seasonal cycle (Fig. 13a) of the Rossby radius slightly (by about 1 km) underestimates the Rossby radius in winter when compared to the individual Argo profiles. Nonetheless, this provides an observationally based estimate of the Rossby radius in the ice-free northern Nordic Seas.

The large Coriolis parameter f and the comparatively weak stratification lead to the small Rossby radius of 2–6 km in the WSC. This contrasts with the 6–10 km observed by ice-tethered profilers (ITPs) in the East Greenland Current (Zhao et al. 2014) where the halocline contribution leads to a larger stratification. Nurser and Bacon (2014) also recently calculated the Rossby radius as the solution of the eigenvalue problem applied to the Polar Science Center Hydrographic Climatology (PHC) climatology (Steele et al. 2001), and values of ≈1 km in winter and ≈3 km in summer in the WSC were found. This was then compared to results from an intermediate-resolution (≈9 km) numerical model. However, the PHC climatology has a moderate horizontal resolution and assumes an idealized nearly sinusoidal seasonal cycle. Also, numerical models at that resolution have trouble simulating the nonzero upper-ocean stratification (Fig. 12a) in winter and may instead have permanently vanishing stratification in winter (T. Hattermann and J. Albretsen 2015, personal communication). This bias only disappears in numerical models with much higher horizontal resolution (e.g., 800 m), thereby justifying the observation-based estimate of the Rossby radius here. We note, however, the significant uncertainties in our method stemming from first using Eq. (5) and then the simplifications applied here to use the upper-ocean stratification from the moorings. Hence, it is not to be expected that the different estimates would agree exactly.

5) EKE PARAMETERIZATIONS

Now we have the tools to assess the amplitude of the seasonal cycle of the EKE resulting from baroclinic instability. For this we consider a linear small-amplitude baroclinic instability that might grow to its final amplitude and then would leave the range of linearity. Furthermore, we assume that this growth occurs in a boundary current and that no EKE is lost from the boundary current in the process. In other words, the EKE is just advected along with the boundary current as it grows in time. Two parameterizations based on these assumptions exist for the expected EKE resulting from baroclinic instability once the instabilities have left the linear regime. We investigate both in order to shed light on whether the physics encapsulated in them can help in

the explanation of the situation in the WSC. Conversely, this study might also be valuable by providing observational numbers on the performance of these parameterizations. Unfortunately, no such parameterizations exist for the EKE generated by barotropic instability.

Stone (1970) showed that the velocity amplitude of the disturbance v' will be the same as the background velocity $\overline{v}$. Using isotropy, EKE is then parameterized as $v'^2 = a\overline{v}^2$, where a is a proportionality factor of the order one. Considering the average background northward velocity (Fig. 5d) in the WSC, $a = \frac{1}{2}$ results in the best fit between the seasonal cycle of EKE observed in the WSC and the Stone (1970) parameterization (Fig. 13b). Another parameterization for the EKE generated by baroclinic instability was introduced by Killworth (1997) and assumes that the eddy velocity scales as the baroclinic growth rate times the deformation radius. The growth rate is the imaginary part ω_i of the complex frequency $\omega = \omega_r + i\omega_i$ of the linear instability problem where the ansatz is made that the solutions to the equations of motion are proportional to $e^{i(\mathbf{kx} - \omega t)}$. Likewise, the frequency of the periodic motion around the eddy center is ω_r, the real part of the complex frequency. The parameterization assumes that the growth rate and the frequency of the periodic motion are of the same order of magnitude for baroclinic instabilities. The length scale over which the periodic motion occurs is the size of an eddy that scales as the Rossby deformation radius. The majority of the EKE is then due to this periodic motion around the eddy centers. The parameterization of Killworth (1997) then again assumes isotropy to find the EKE as $v'^2 = b\omega^2 R_d^2$, where b is another order-one proportionality factor. Using our estimates of the growth rate (Fig. 12d) and the Rossby radius (Fig. 13a), the best agreement between the parameterized EKE (Fig. 13b) and the observed EKE in the WSC is obtained for $b = \frac{1}{4}$.

Both of these parameterizations reproduce the shape of the seasonal cycle of the EKE well, and in both cases the proportionality factors are ≤1. Hence, baroclinic instability of the boundary current likely produced the EKE. But the fact that the parameterizations slightly overestimate the EKE suggests that either the instability has not grown to final amplitude or some, but not most, of the EKE has been lost from the boundary current. The first scenario could happen if the advective velocity was too large, resulting in a short transit time through the region where the current was unstable. Here, we can only analyze the stability of the boundary current at the mooring array location, but the bathymetry (Fig. 11) and the satellite-derived EKE (Fig. 9) suggest that the stability characteristics are similar along most of the West Spitsbergen margin south of 79°N. From 77°N to the

mooring array, the advective time is ≈12 days, that is, many growth periods, and hence, it is unlikely that the water in the boundary current is advected through the unstable region in such a short time that these quickly growing instabilities would not have had time to grow to final amplitude. On the other hand, EKE can be lost from the boundary current through cross-stream eddy fluxes and the westward-flowing recirculation, and the satellite-derived EKE (Fig. 9) suggests that this may especially occur from 78°30′N onward. This would be consistent with the slightly lower values that are observed than what the parameterizations suggest. Additionally, this assumes that the eddy field is baroclinic and the maximum amplitude is near the surface consistent with the parameterizations.

The ratio of the winter to summer EKE determined by the Killworth (1997) parameterization is slightly lower than in the observations. This may be because barotropic instability also appears to contribute to the EKE generated in winter. Recall that the energy conversions (Fig. 10) show that barotropic instability is present but weaker than baroclinic instability and that Teigen et al. (2010) found the conditions for barotropic instability in the WSC to be fulfilled about 60% of the time. This would suggest that barotropic instability probably contributes around 20% to the EKE in winter.

6. Conclusions

a. Summary

The 16 yr current and temperature–salinity measurements from moorings in the WSC at 78°50′N were analyzed for the nature of mesoscale fluctuations and for the possibility of their generation through instabilities of the WSC. We found a strong seasonality of the mesoscale EKE in the boundary current and in the central Fram Strait, and independent arguments support that this EKE is generated by the instability of the boundary current. High-frequency local wind forcing is not required to explain the level of EKE. In winter, water is advected in the current that has been cooled upstream and as a result the stratification in the top 250 m is weak; likewise, the wind forcing of the gyre circulation is stronger, and hence the velocity in the WSC is stronger compared to summer and has a greater vertical shear. This favors the baroclinic instability of the current in winter and the formation of eddies, since it gives rise to a baroclinic e-folding growth period of about half a day in winter. In summer the current and its shear is weaker, and because the surface waters have not been cooled significantly in the Nordic Seas, its stratification in the top 250 m is large. Therefore, the summer WSC is

significantly less unstable; it has an e-folding growth period for baroclinic instabilities of 2 days and thus forms fewer eddies and the total generated EKE is weaker. Parameterizations for the expected final EKE based on the mean flow as well as on the baroclinic growth rate and the Rossby radius correctly reproduce the observed EKE values. In winter, barotropic instability also contributes to the EKE generation. The observed EKE in Fram Strait has a maximum in the boundary current in January–February when it is most unstable. Thereafter, the eddies are likely advected westward, and the EKE maximum observed 1–2 months later in the central Fram Strait may plausibly be due to the advected eddies. That is, eddy advection would lead to the amplitude, timing, and baroclinic nature of the EKE observed in the central Fram Strait. By contrast, the EKE in the boundary current as well as in the central Fram Strait is reduced by a factor of more than 3 in late summer (August–September).

b. Discussion

What are the consequences of the seasonal cycle of mesoscale instability of boundary currents? In the West Greenland Current in the eastern Labrador Sea, the seasonal EKE signal was reproduced by a numerical model solely forced with monthly mean winds (Eden and Böning 2002). The model produces the changing flow speeds over the seasons, and these changing flow speeds alter the strength of the instability (Eden and Böning 2002). This contrasts with earlier studies that found that the high-frequency winds correlated with the EKE maxima. The conclusion was that the winds indirectly influence the flow field and the EKE but that the high-frequency oceanic variability in the West Greenland Current does not depend on the high-frequency variability of the winds. Instead, it is generated by oceanic processes. The seasonal cycle of the stability of the Labrador Current in the western Labrador Sea is related to the stratification. The much reduced stratification associated with open-ocean convection offshore of the current in winter results in significantly greater baroclinic growth rates of the current in winter than in summer, corresponding well with the higher EKE observed at that time (Thomsen et al. 2014). Based on our results, we believe that the situation in the WSC is similar and that the differing instability levels between the seasons are the reason for the different levels of observed EKE.

Another interpretation for why the EKE level is so much smaller in summer in the WSC would be that the offshore branch of the WSC is weak in summer (Figs. 2b, 5d). If the baroclinic instability mainly occurs in the offshore branch, its significant transport reduction

would also greatly reduce the overall EKE generation in the WSC in summer. Conversely, during the seasons that the offshore branch is present, it is unstable and generates a lot of EKE.

What is the ultimate cause of this local mesoscale situation observed in the WSC? The air–sea interaction over the Nordic Seas is stronger in winter. The stronger wind stress curl over the Nordic Seas in winter leads to a spinup of the cyclonic gyre circulation of the Nordic Seas (Isachsen et al. 2003; Voet et al. 2010) that manifests itself in the stronger flow in the WSC in winter. This especially explains the increased flow in the offshore branch that is more closely related to the gyre circulation than the flow near the West Spitsbergen shelf break and causes an increase in recirculation in central Fram Strait in winter (de Steur et al. 2014). Similarly, the air–sea heat fluxes over the Nordic Seas are much stronger in winter than in summer (Simonsen and Haugan 1996; Schlichtholz and Houssais 2011), and this is the reason for the hydrographic structure of the Atlantic Water (AW) in the WSC in the different seasons. The weak stratification in winter is a result of the intense winter cooling that the water has been subjected to in the Nordic Seas. Conversely, the weak atmospheric fluxes in summer allow for the temperature-stratified AW to enter Fram Strait. This means that the mesoscale variability is locally generated in Fram Strait but that the conditions that foster the greater generation of variability in winter compared to summer are set by the air–sea interaction over the much larger area of the Nordic Seas. This is similar to the situation in the Labrador Sea (Eden and Böning 2002; Thomsen et al. 2014) but different from some other locations in the world oceans where the mesoscale variability is locally forced by atmospheric storm systems.

The transport of oceanic heat into the Arctic Ocean through Fram Strait has been of interest for a long time (e.g., Fahrbach et al. 2001; Schauer et al. 2004, 2008). The amount of warm AW that flows northward at the 78°50′N array is well observed. However, it is not clear how much warm AW, and at what temperature and depth, continues to flow northward and into the Arctic Ocean proper and how much of it, and at what temperature and depth, recirculates westward toward Greenland. This is one of the major problems for determining the oceanic heat flux into the Arctic Ocean. This study aimed to increase the understanding of the dynamical processes contributing to the recirculation. One of these is that the boundary current is unstable and thereby might lose volume and heat by westward eddy fluxes. Disregarding the theoretical problems with defining heat fluxes from observations related to reference temperature and situations of nonzero net mass flux

(Schauer and Beszczynska-Möller 2009), zonal eddy heat fluxes are proportional to $\overline{u'T'}$. The variability of the zonal flow u' is larger in winter (larger EKE; Fig. 8). Meanwhile, the temperature difference between the warmer boundary current and the water outside of the boundary current is larger in summer (Fig. 4b), which probably leads to a larger variability in the instantaneous temperature T'. Therefore, these two effects act in opposite ways, and it is not obvious whether the zonal eddy heat fluxes are greater in summer or winter or whether they do not change significantly between the seasons. This warrants an explicit quantification of the zonal eddy fluxes in the future.

Downstream of the WSC, north of Svalbard, the AW near the surface is transformed by the interaction with sea ice to form the halocline (Rudels et al. 2005). During this process, water is not subducted, as is stated sometimes, but the water properties (temperature and salinity) are modified and a new water mass is formed. The situation in the recirculation area in the central Fram Strait is different. There Atlantic Water actually moves underneath the polar water flowing out of the Arctic Ocean. It has been speculated (Hattermann et al. 2016, manuscript submitted to *Geophys. Res. Lett.*) that eddies are essential to the vertical motion of the AW that started out at the surface in the WSC but is found underneath the polar outflow in the central and western Fram Strait. The instability mechanisms discussed here are a likely source of those eddies.

REFERENCES

Aagaard, K., A. Foldvik, and S. Hillman, 1987: The West Spitsbergen Current: Disposition and water mass transformation. *J. Geophys. Res.*, **92**, 3778–3784, doi:10.1029/JC092iC04p03778.

Aksenov, Y., V. Ivanov, A. Nurser, S. Bacon, I. Polyakov, A. Coward, A. Naveira-Garabato, and A. Beszczynska-Möller, 2011: The Arctic Circumpolar Boundary Current. *J. Geophys. Res.*, **116**, C09017, doi:10.1029/2010JC006637.

AVISO, 2015: AVISO Satellite Altimetry Data: SSALTO/DUACS multimission altimeter products. AVISO, accessed 26 September 2015. [Available online at http://www.aviso.altimetry.fr/duacs/].

Bauerfeind, E., and Coauthors, 2009: Particle sedimentation patterns in the eastern Fram Strait during 2000–2005: Results from the Arctic long-term observatory HAUSGARTEN. *Deep-Sea Res. I*, **56**, 1471–1487, doi:10.1016/j.dsr.2009.04.011.

——, A. Beszczynska-Möller, W.-J. von Appen, T. Soltwedel, B. Sablotny, and N. Lochthofen, 2015: Physical oceanography and current meter data from moorings at HAUSGARTEN, 2001–2014. PANGAEA, accessed 26 September 2015, doi:10.1594/PANGAEA.150005.

Beszczynska-Möller, A., E. Fahrbach, U. Schauer, and E. Hansen, 2012: Variability in Atlantic water temperature and transport at the entrance to the Arctic Ocean, 1997–2010. *ICES J. Mar. Sci.*, **69**, 852–863, doi:10.1093/icesjms/fss056.

——, W.-J. von Appen, and E. Fahrbach, 2015: Physical oceanography and current meter data from moorings F1-F14 and F15/F16 in the Fram Strait, 1997-2012. PANGAEA, accessed 26 September 2015, doi:10.1594/PANGAEA.150016.

Bourke, R., A. Weigel, and R. Paquette, 1988: The westward turning branch of the West Spitsbergen Current. *J. Geophys. Res.*, **93**, 14 065–14 077, doi:10.1029/JC093iC11p14065.

Boyd, T. J., and E. A. D'Asaro, 1994: Cooling of the West Spitsbergen Current: Wintertime observations west of Svalbard. *J. Geophys. Res.*, **99**, 22 597–22 618, doi:10.1029/94JC01824.

Bulczak, A. I., S. Bacon, A. C. Naveira Garabato, A. Ridout, M. J. Sonnewald, and S. W. Laxon, 2015: Seasonal variability of sea surface height in the coastal waters and deep basins of the Nordic Seas. *Geophys. Res. Lett.*, **42**, 113–120, doi:10.1002/2014GL061796.

Chelton, D. B., R. A. Deszoeke, M. G. Schlax, K. El Naggar, and N. Siwertz, 1998: Geographical variability of the first baroclinic Rossby radius of deformation. *J. Phys. Oceanogr.*, **28**, 433–460, doi:10.1175/1520-0485(1998)028<0433:GVOTFB>2.0.CO;2.

de Steur, L., E. Hansen, R. Gerdes, M. Karcher, E. Fahrbach, and J. Holfort, 2009: Freshwater fluxes in the East Greenland Current: A decade of observations. *Geophys. Res. Lett.*, **36**, L23611, doi:10.1029/2009GL041278.

——, ——, C. Mauritzen, A. Beszczynska-Möller, and E. Fahrbach, 2014: Impact of recirculation on the East Greenland Current in Fram Strait: Results from moored current meter measurements between 1997 and 2009. *Deep-Sea Res.*, **92**, 26–40, doi:10.1016/j.dsr.2014.05.018.

Eady, E., 1949: Long waves and cyclone waves. *Tellus*, **1A**, 33–52, doi:10.1111/j.2153-3490.1949.tb01265.x.

Eden, C., and C. Böning, 2002: Sources of eddy kinetic energy in the Labrador Sea. *J. Phys. Oceanogr.*, **32**, 3346–3363, doi:10.1175/1520-0485(2002)032<3346:SOEKEI>2.0.CO;2.

Fahrbach, E., J. Meincke, S. Østerhus, G. Rohardt, U. Schauer, V. Tverberg, and J. Verduin, 2001: Direct measurements of volume transports through Fram Strait. *Polar Res.*, **20**, 217–224, doi:10.1111/j.1751-8369.2001.tb00059.x.

Gascard, J.-C., C. Richez, and C. Rouault, 1995: New insights on large-scale oceanography in Fram Strait: The West Spitsbergen Current. *Arctic Oceanography: Marginal Ice Zones and Continental Shelves*, W. O. Smith and J. M. Grebmeir, Eds., Coastal and Estuarine Studies Series, Vol. 49, Amer. Geophys. Union, 131–182.

Hanzlick, D., 1984: The West Spitsbergen Current: Transport, forcing, and variability. Ph.D. thesis, University of Washington, 140 pp.

Heorton, H. D., D. L. Feltham, and J. C. Hunt, 2014: The response of the sea ice edge to atmospheric and oceanic jet formation. *J. Phys. Oceanogr.*, **44**, 2292–2316, doi:10.1175/JPO-D-13-0184.1.

IBCAO, 2015: International Bathymetric Chart of the Arctic Ocean: Technical references & sources. IBCAO, accessed 26 September 2015. [Available online at http://www.ngdc.noaa.gov/mgg/bathymetry/arctic/tech_sources.html.]

Isachsen, P. E., J. LaCasce, C. Mauritzen, and S. Häkkinen, 2003: Wind-driven variability of the large-scale recirculating flow in the Nordic Seas and Arctic Ocean. *J. Phys. Oceanogr.*, **33**, 2534–2550, doi:10.1175/1520-0485(2003)033<2534:WVOTLR>2.0.CO;2.

Jakobsson, M., and Coauthors, 2012: The International Bathymetric Chart of the Arctic Ocean (IBCAO) version 3.0. *Geophys. Res. Lett.*, **39**, L12609, doi:10.1029/2012GL052219.

Johannessen, J., and Coauthors, 1987: Mesoscale eddies in the Fram Strait marginal ice zone during the 1983 and 1984 Marginal Ice Zone Experiments. *J. Geophys. Res.*, **92**, 6754–6772, doi:10.1029/JC092iC07p06754.

Johannessen, O., J. Johannessen, J. Morison, B. Farrelly, and E. Svendsen, 1983: Oceanographic conditions in the marginal ice zone north of Svalbard in early fall 1979 with an emphasis on mesoscale processes. *J. Geophys. Res.*, **88**, 2755–2769, doi:10.1029/JC088iC05p02755.

Jónsson, S., A. Foldvik, and K. Aagaard, 1992: The structure and atmospheric forcing of the mesoscale velocity field in Fram Strait. *J. Geophys. Res.*, **97**, 12 585–12 600, doi:10.1029/92JC01195.

Killworth, P. D., 1997: On the parameterization of eddy transfer. Part I. Theory. *J. Mar. Res.*, **55**, 1171–1197, doi:10.1357/0022240973224102.

Latarius, K., and D. Quadfasel, 2010: Seasonal to inter-annual variability of temperature and salinity in the Greenland Sea Gyre: Heat and freshwater budgets. *Tellus*, **62A**, 497–515, doi:10.1111/j.1600-0870.2010.00453.x.

Lilly, J., P. Rhines, F. Schott, K. Lavender, J. Lazier, U. Send, and E. D'Asaro, 2003: Observations of the Labrador Sea eddy field. *Prog. Oceanogr.*, **59**, 75–176, doi:10.1016/j.pocean.2003.08.013.

Manley, T., K. Hunkins, J. Villanueva, J. Van Leer, J. Gascard, and P. Jeannin, 1987: Mesoscale oceanographic processes beneath the ice of Fram Strait. *Science*, **236**, 432–434, doi:10.1126/science.236.4800.432.

Marnela, M., B. Rudels, M.-N. Houssais, A. Beszczynska-Möller, and P. Eriksson, 2013: Recirculation in the Fram Strait and transports of water in and north of the Fram Strait derived from CTD data. *Ocean Sci.*, **9**, 499–519, doi:10.5194/os-9-499-2013.

Nilsen, F., B. Gjevik, and U. Schauer, 2006: Cooling of the West Spitsbergen Current: Isopycnal diffusion by topographic vorticity waves. *J. Geophys. Res.*, **111**, C08012, doi:10.1029/2005JC002991.

NCDC, 2015: NOAA/National Climatic Data Center: Optimally interpolated daily AVHRR-AMSR sea surface temperature version 2. National Climatic Data Center, accessed 26 September 2015. [Available online at ftp://eclipse.ncdc.noaa.gov/pub/OI-daily-v2/NetCDF/.]

NODC, 2015: NOAA/National Centers for Environmental Information: Argo floats data. National Oceanographic Data Center, accessed 26 September 2015. [Available online at https://www.nodc.noaa.gov/argo/floats_data.htm.]

Nurser, A., and S. Bacon, 2014: The Rossby radius in the Arctic Ocean. *Ocean Sci.*, **10**, 967–975, doi:10.5194/os-10-967-2014.

Quadfasel, D., J.-C. Gascard, and K.-P. Koltermann, 1987: Large-scale oceanography in Fram Strait during the 1984 Marginal Ice Zone Experiment. *J. Geophys. Res.*, **92**, 6719–6728, doi:10.1029/JC092iC07p06719.

Reynolds, R. W., T. M. Smith, C. Liu, D. B. Chelton, K. S. Casey, and M. G. Schlax, 2007: Daily high-resolution-blended analyses for sea surface temperature. *J. Climate*, **20**, 5473–5496, doi:10.1175/2007JCLI1824.1.

Rudels, B., E. Jones, L. Anderson, and G. Kattner, 1994: On the intermediate depth waters of the Arctic Ocean. *The Polar Oceans and Their Role in Shaping the Global Environment*, Geophys. Monogr., Vol. 85, Amer. Geophys. Union, 33–46.

——, H. Friedrich, and D. Quadfasel, 1999: The Arctic circumpolar boundary current. *Deep-Sea Res. II*, **46**, 1023–1062, doi:10.1016/S0967-0645(99)00015-6.

——, G. Björk, J. Nilsson, P. Winsor, I. Lake, and C. Nohr, 2005: The interaction between waters from the Arctic Ocean and the Nordic Seas north of Fram Strait and along the East Greenland Current: Results from the Arctic Ocean-02 Oden expedition. *J. Mar. Syst.*, **55**, 1–30, doi:10.1016/j.jmarsys.2004.06.008.

Schauer, U., and A. Beszczynska-Möller, 2009: Problems with estimation and interpretation of oceanic heat transport— Conceptual remarks for the case of Fram Strait in the Arctic Ocean. *Ocean Sci.*, **5**, 487–494, doi:10.5194/os-5-487-2009.

——, E. Fahrbach, S. Osterhus, and G. Rohardt, 2004: Arctic warming through the Fram Strait: Oceanic heat transport from 3 years of measurements. *J. Geophys. Res.*, **109**, C06026, doi:10.1029/2003JC001823.

——, A. Beszczynska-Möller, W. Walczowski, E. Fahrbach, J. Piechura, and E. Hansen, 2008: Variation of measured heat flow through the Fram Strait between 1997 and 2006. *Arctic-Subarctic Ocean Fluxes*, R. R. Dickson, J. Meincke, and P. Rhines, Eds., Springer, 65–85.

Schlichtholz, P., and M.-N. Houssais, 2011: Forcing of oceanic heat anomalies by air-sea interactions in the Nordic Seas area. *J. Geophys. Res.*, **116**, C01006, doi:10.1029/2009JC005944.

Simonsen, K., and P. M. Haugan, 1996: Heat budgets of the Arctic Mediterranean and sea surface heat flux parameterizations for the Nordic Seas. *J. Geophys. Res.*, **101**, 6553–6576, doi:10.1029/95JC03305.

Spall, M. A., 2011: On the role of eddies and surface forcing in the heat transport and overturning circulation in marginal seas. *J. Climate*, **24**, 4844–4858, doi:10.1175/2011JCLI4130.1.

——, and J. Pedlosky, 2008: Lateral coupling in baroclinically unstable flows. *J. Phys. Oceanogr.*, **38**, 1267–1277, doi:10.1175/2007JPO3906.1.

——, R. S. Pickart, P. Fratantoni, and A. Plueddemann, 2008: Western Arctic shelfbreak eddies: Formation and transport. *J. Phys. Oceanogr.*, **38**, 1644–1668, doi:10.1175/2007JPO3829.1.

Spreen, G., L. Kaleschke, and G. Heygster, 2008: Sea ice remote sensing using AMSR-E 89-GHz channels. *J. Geophys. Res.*, **113**, C02S03, doi:10.1029/2005JC003384.

Steele, M., R. Morley, and W. Ermold, 2001: PHC: A global ocean hydrography with a high-quality Arctic Ocean. *J. Climate*, **14**, 2079–2087, doi:10.1175/1520-0442(2001)014<2079:PAGOHW>2.0.CO;2.

Stone, P. H., 1970: On non-geostrophic baroclinic stability: Part II. *J. Atmos. Sci.*, **27**, 721–726, doi:10.1175/1520-0469(1970)027<0721:ONGBSP>2.0.CO;2.

Teigen, S., F. Nilsen, and B. Gjevik, 2010: Barotropic instability in the West Spitsbergen Current. *J. Geophys. Res.*, **115**, C07016, doi:10.1029/2009JC005996.

——, ——, R. Skogseth, B. Gjevik, and A. Beszczynska-Möller, 2011: Baroclinic instability in the West Spitsbergen Current. *J. Geophys. Res.*, **116**, C07012, doi:10.1029/2011JC006974.

Thomsen, S., C. Eden, and L. Czeschel, 2014: Stability analysis of the Labrador Current. *J. Phys. Oceanogr.*, **44**, 445–463, doi:10.1175/JPO-D-13-0121.1.

University of Bremen, 2015a: Institute of Environmental Physics, University of Bremen: Daily AMSR-E sea ice maps. University of Bremen, accessed 26 September 2015. [Available online at http://www.iup.uni-bremen.de/seaice/amsr/.]

——, 2015b: Institute of Environmental Physics, University of Bremen: daily AMSR2 sea ice maps. University of Bremen, accessed 26 September 2015. [Available online at http://www.iup.uni-bremen.de:8084/amsr2/.]

Vallis, G. K., 2006: *Atmospheric and Oceanic Fluid Dynamics: Fundamentals and Large-Scale Circulation*. Cambridge University Press, 745 pp.

Voet, G., D. Quadfasel, K. Mork, and H. Søiland, 2010: The mid-depth circulation of the Nordic Seas derived from profiling float observations. *Tellus*, **62A**, 516–529, doi:10.1111/j.1600-0870.2010.00444.x.

von Appen, W.-J., U. Schauer, R. Somavilla Cabrillo, E. Bauerfeind, and A. Beszczynska-Möller, 2015a: Physical oceanography during various cruises to the Fram Strait. PANGAEA, accessed 26 September 2015, doi:10.1594/PANGAEA.150007.

——, ——, ——, ——, and ——, 2015b: Exchange of warming deep waters across Fram Strait. *Deep-Sea Res.*, **103**, 86–100, doi:10.1016/j.dsr.2015.06.003.

Walczowski, W., and J. Piechura, 2007: Pathways of the Greenland Sea warming. *Geophys. Res. Lett.*, **34**, L10608, doi:10.1029/2007GL029974.

Woodgate, R., K. Aagaard, R. Muench, J. Gunn, G. Bjork, B. Rudels, A. Roach, and U. Schauer, 2001: The Arctic Ocean boundary current along the Eurasian slope and the adjacent Lomonosov Ridge: Water mass properties, transports and transformations from moored instruments. *Deep-Sea Res. I*, **48**, 1757–1792, doi:10.1016/S0967-0637(00)00091-1.

Zeng, L., and G. Levy, 1995: Space and time aliasing structure in monthly mean polar-orbiting satellite data. *J. Geophys. Res.*, **100**, 5133–5142, doi:10.1029/94JD03252.

Zhao, M., M.-L. Timmermans, S. Cole, R. Krishfield, A. Proshutinsky, and J. Toole, 2014: Characterizing the eddy field in the Arctic Ocean halocline. *J. Geophys. Res. Oceans*, **119**, 8800–8817, doi:10.1002/2014JC010488.